Charles University in Prague
Faculty of Mathematics and Physics

DIPLOMA THESIS

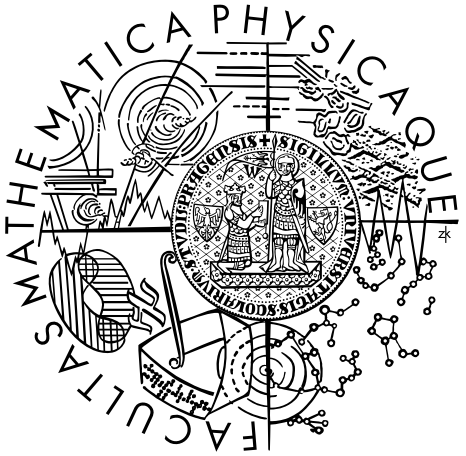

Bc. Vít Beran

Parametrized model of a cooling magma reservoir

Department of Geophysics

Supervisor of the master thesis: RNDr. Vojtěch Patočka, PhD.

Study programme: Physics

Study branch: Geophysics and Physics of Planets

Prague 2024

I declare that I carried out this master thesis independently, and only with the cited sources, literature and other professional sources.

I understand that my work relates to the rights and obligations under the Act No. 121/2000 Sb., the Copyright Act, as amended, in particular the fact that the Charles University in Prague has the right to conclude a license agreement on the use of this work as a school work pursuant to Section 60 subsection 1 of the Copyright Act.

In ..... date ..... signature of the author

Title: Parametrized model of a cooling magma reservoir

Author: Bc. Vít Beran

Department: Department of Geophysics

Supervisor: RNDr. Vojtěch Patočka, PhD, Department of Geophysics

Abstract: With the aim to better understand the solidification process of igneous intrusions, we develop a numerical model for computing crystal size distributions in an under-cooled magma. Assuming a magma chamber that consists of a well-mixed bulk, capped by a thermal boundary layer, we simulate crystal nucleation, growth, and settling, hence sediment formation within the system. The model is endowed with realistic, temperature-dependent crystallization kinetics, and incorporates complex dynamics of inertial particles in a convecting fluid, i.e. crystal settling, in a parametrized form. We developed a custom-made numerical code in *Python 3* and performed a series of simulations studying the imprint of convection vigor in the resulting distributions, and compared some basic aspects of the obtained microstructure with observations. Finally, we outline a theoretical concept of how to couple the presented model with a self-consistently computed thermal evolution of the temperature inside the chamber.

Keywords: magma crystallization intrusion parametrized model

I want to express my gratitude to my supervisor doctor Vojtěch Patočka for his guidance and help with the thesis. I also thank my family for both moral and financial support during my studies, my tomcat Vexille for the cuddles, and my closest friends for the joyful moments and laughter.

Contents

Introduction

The idea that bodies of liquid magma reside beneath the Earth's surface can be traced back more than a century ago and has evolved significantly over time. Initially, the concept of subsurface magma chambers was created to explain geological observations such as volcanism, the origin of igneous rocks, or the existence of calderas. Eventually, the concept of a magma chamber as a large tank-like reservoir, either supplying volcanoes or being emplaced in crustal rock, gained widespread recognition (big tank hypothesis). With the advent of seismic measurements, however, it became evident that fully liquid chambers in the crust are far less frequent than anticipated (e.g., Sinton and Detrick [1992]). Instead, it is now believed that most magma chambers comprise isolated lens of magma, connected by mushy regions and veined piping. Nevertheless, there are examples of large igneous intrusions (e.g., the Sierra Nevada batholith) and a number of layered intrusions (e.g., Skaergaard in Greenland) that fulfill the traditional definition of a magma chamber.

Magma is typically generated in the upper mantle or lower crust (e.g., Frank Press [2000]), where temperature and pressure are high enough to partially melt the antecedent rock. The less dense melt slowly ascends upwards through cracks and faults until it eventually becomes trapped in a pre-existing cavity or a weak zone. Once emplaced, magma starts to cool and solidify. Eventually, it reaches the ambient temperature, and the solid igneous rock (e.g., sill, dike, batholith,..) can either remain buried beneath the surface of Earth, or become exposed at the surface through the process of erosion.

When hot magma is emplaced, it loses heat to the surrounding host rock, and a question arises as to whether thermal convection occurs within the liquid. This very question was investigated several decades ago in a number of studies. At the turn of the 1990s, renowned petrologist and geologist Bruce D. Marsh published a series of exhaustive papers addressing fluid dynamics in magma chambers and its implications for their thermal evolution (Marsh [1990], Marsh [1989a], and Marsh [1989b]). His conclusions sparked a discussion by geophysicists and fluid dynamicists Herbert E. Huppert and J. Stewart Turner on the vigor of thermal convection in magma chambers (Huppert and Turner [1991] and Marsh [1991]). While Marsh argued that convection in nearly all magma chambers is weak or ceases within a short time and is thus limited to the very early stage of the solidification process, and grounded his arguments in low-temperature analogue experiments (Brandeis and Marsh [1989]), Huppert and Turner based their stance purely on the axiomatic concepts of fluid mechanics and pointed out several physical inconsistencies in Marsh's thesis and they show, to the contrary, that the convection style inside a typical magma chamber is long-lived and highly turbulent. Both sides agreed that of key interest are the temperature and/or compositional contrasts driving convection within the magma, and that the contrasts are expected to be small. The question of how small, however, remains unresolved as there are no direct measurements of the system. The estimates in the aforementioned competing papers differ by orders of magnitude, with Marsh arguing for the temperature contrast being only a tiny fraction of one degree Kelvin.

The aim of this thesis is to address magma chamber dynamics through the size

distribution of crystals in the cumulate, i.e. through the micro-structure of the already solidified intrusions. Once nucleated, solid crystals are expected to undergo gravitational settling, and the settling dynamics are quite different depending on whether the background magma is convecting or not. When the crystal size distribution is predicted for magmas with a different convective vigor, ranging from static to highly turbulent, one can make comparisons with observations and infer the magma dynamics a posteriori.

Despite the fact that igneous complexes host deposits of economically important resources, our understanding of their solidification remains strikingly poor. Two fundamentally different formation mechanisms are typically considered: i) solidification via crystal settling: nucleated crystals are suspended in the interior fluid where they grow in size and settle at the base of the chamber, and ii) in-situ crystallization, a scenario in which the chamber solidifies from the walls inwards and no crystal transport is involved. The latter scenario is favoured by many petrologists. In order to distinguish between the two, one must know what sort of signature the different mechanisms leave in the observable microstructure. To this end, we investigate the first scenario in this thesis.

Since observations from layered intrusions were inconclusive and no experimental work on particle settling in vigorously convective systems had been performed at that time, D. Martin and R. Nokes conducted their own experiments at the end of the 1980s (Martin and Nokes [1988] and Martin and Nokes [1989]). They studied the settling of tiny polystyrene particles in turbulent systems (with Rayleigh numbers $Ra \gtrsim 10^7$, see Fig. 1) cooled from above, and discovered a simple yet robust theory, which could be applied to small crystals in magmas with low kinematic viscosities.

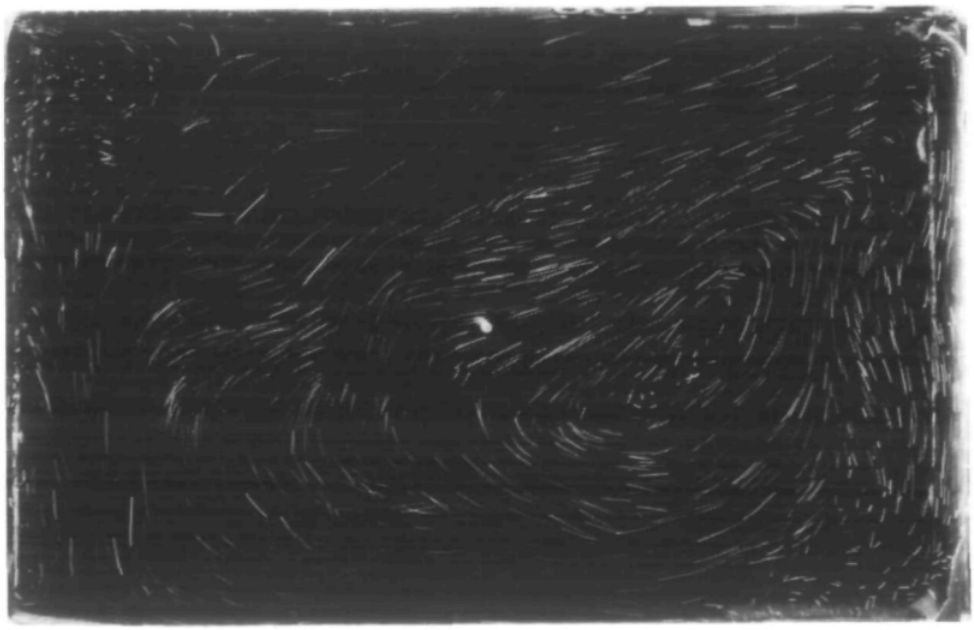

Figure 1: Photograph of one of the experiments by Martin and Nokes showing convecting style for Rayleigh number $Ra = 2 \times 10^8$ and Prandtl number $Pr = 7$, cooled from above. Adopted from Martin and Nokes [1989].

Later, Patočka et al. [2022] performed 3D numerical experiments and derived a formula that captures the residence time of both turbulently mixed particles and those with nearly vertical trajectories, with the free parameter being the ratio of particle Stokes velocity to the mean velocity of the background flow. With an analytical formula that describes the settling dynamics of variously sized particles at hand, one can construct a parametrized model of the solidification process.

During the solidification, the composition of magma evolves in time, following Bowen's reaction series, which predicts what mineral phases form concurrently. The widespread recognition of Bowen's reaction series in natural samples was one of the reasons why the big tank hypothesis became a popular concept in the textbook explanation of igneous intrusions.

While much literature is devoted to the petrology and to the crystallization sequence of magma in particular, less common are works that address the solidification dynamics with the help of a physics-based model. To our knowledge, the only attempt to build a parameterized model of a convecting magma chamber that accounted for crystal growth kinetics – thus having the ability to predict the crystal size distribution of the resulting intrusion – can be attributed to Jarvis and Woods [1994]. They combine a theoretical model of thermal convection with the settling theory of Martin and Nokes, and employ linear kinetic laws for crystal nucleation and growth. Their study, however, was limited to a qualitative analysis of the system and the results were presented in a dimensionless form, which prohibited the paper from reaching a broader geological audience. Moreover, the settling dynamics and the crystal growth kinetics were too simplistic in view of the present-day understanding of these phenomena. In this thesis, we expand the work of Jarvis and Woods, in particular by accounting for more realistic crystal growth kinetics and settling dynamics.

The model presented here uses boundary layer theory to predict the temperature profile in a convecting magma (following Jarvis and Woods [1994]), and employs realistic kinetic laws (Hort [1997]) to estimate the nucleation and growth of crystals within the liquid. To compute how the crystal size distribution in the convecting bulk is filtered in the process of sediment formation, the settling dynamics after Martin and Nokes [1988] and Patočka et al. [2022] are invoked.

It should be noted here that the solidification process of natural magma chambers is extremely complex and there is a list of effects that our model does not account for - e.g., petrological evolution, (periodic) injection of magma with a different composition, re-entrainment (crystals from the uppermost layer of the sediment pile may get swept back into the suspension). There is also a number of post-cumulus effects such as Oswald ripening (smaller particles tend to dissolve because they have a higher surface energy compared to larger particles) or solidification of the interstitial melt, which makes the hypothetical signature of the crystal settling more difficult to identify. Some magma chambers might have also been impacted by catastrophic scenarios (e.g., roof collapse) in the past – such events can completely throw the settling dynamics signature into disarray.

Nevertheless, analysis of microstructure seems to be a promising tool to gain insight into the processes that formed igneous rocks. For example, the measurement and counting of olivine crystals in a series of samples from the Shiant Isle Main Sill lead Holness et al. [2017] to speculate that the olivine cargo was stirred by convecting motions before forming the deposit (Fig. 2, cf. also Holness [2022]).

Moreover, with the recent advancements in machine learning and image recognition, microstructural analysis may potentially experience significant progress in the upcoming years, but without predicted signatures to look for, its ability to decipher the formation history will be limited.

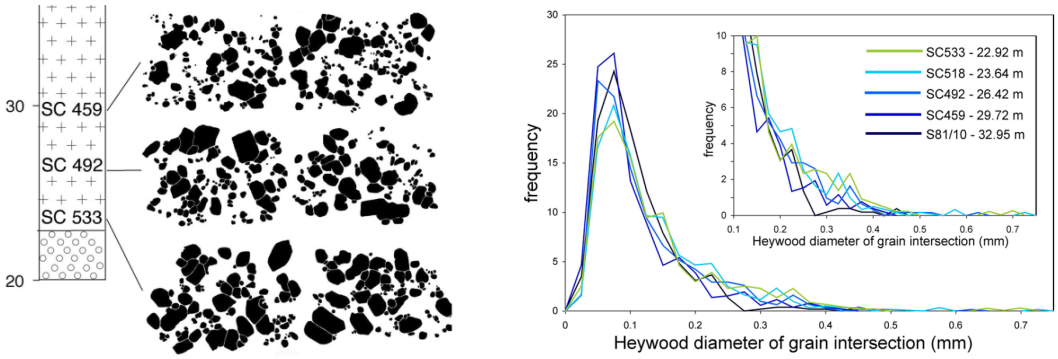

Figure 2: Microstructure of the Shiant Isles Main Sill. Right panel shows how the crystal size distribution in the sediment varies with height, adopted from Holness et al. [2017].

In conclusion, the here constructed model attempts to do the following: *if* the primary mechanism of sediment formation is crystal settling, we seek answers to the subsequent queries:

- What is the crystal size distribution in the sediment for a given convective vigor in a magma chamber of a given height? What values of the mean crystal radius do we predict?
- Do we observe a unique signature of convective vigor in the sediment? Can we distinguish different modes of crystal settling dynamics?
- What are the typical time scales of the individual processes taking part? What is the predicted rate of sedimentation?
- How does the mean crystal radius evolve with depth in the cumulate pile? Does it tell us anything about the thermal history of the body?

The following text is split into four chapters. The first chapter establishes the parameterized model and introduces kinetic laws, the second chapter describes the numerical implementation of individual phases of the model, followed by the third chapter, which covers our results and basic interpretation. In the fourth chapter, we outline the future ambitions and propose a theoretical model to realistically model the thermal evolution of the chamber.

1. Parametrized model

In this chapter, the physical model is introduced. In the initial state, the entire volume of the chamber of height H_0 contains a fully liquid magma. As the liquid cools down, thermal convection inside the chamber is initiated and eventually there will be regions with undercooling sufficient for crystal nucleation. The nucleated crystals will grow in size and eventually settle at the base of the chamber, forming a sediment pile of height h. The Rayleigh-Bénard convection of the fluid can be described by the following dimensionless quantities - Rayleigh and Prandtl numbers, defined as

$$Ra = \frac{g_0 \alpha \Delta T (H_0 - h)^3}{\nu \kappa}\,, \tag{1.1}$$

$$Pr = \frac{\nu}{\kappa}\,, \tag{1.2}$$

where g_0 is the gravitational acceleration, α denotes the thermal expansivity, κ and ν denote the diffusivity and kinematic viscosity of the liquid magma, respectively. The Rayleigh number measures the ratio of buoyant forces to viscous and thermal diffussion, i.e. it is a ratio of the forces driving the flow to the forces opposing it and hence it determines the convective vigor. The Prandtl number is essentially a material parameter comparing the kinematic viscosity and thermal diffusivity of the substance, relating the diffusion of inertia with the thermal diffusion.

Due to the low viscosity of magma, Rayleigh number may attain high values in magma chambers (evaluating Eq. (1.1) for sample values $H_0 - h \sim 10^3$ m and $\Delta T \sim 1$ K yields $Ra \sim 10^{15}$, other material constants are listed in Tab. 3.1). In vigorously convecting systems, strong temperature gradients develop in thin thermal boundary layers at horizontal walls, while the convecting interior (henceforth termed convecting bulk) maintains a uniform temperature T_B due to efficient mixing (e.g., Turcotte and Schubert [2014]).

When magma is emplaced into the host rock, the host rock is colder and therefore a thermal boundary layer should develops at both the top and bottom boundaries of the chamber. However, we assume that the sediment pile accumulates fast enough such as to insulate the liquid from the wall rock at the base. Therefore, we assume the temperature profile to resemble that of a system cooled solely from above, with zero heat flux at the bottom (see Fig. 1.1). The thermal contrast driving convection is defined as $\Delta T = T_B - T_R$, where T_R is the temperature at the roof of the chamber. Throughout most of the thesis, T_B and ΔT are free parameters that we prescribe and study how the resulting crystal distribution depends on the selected values. In Chapter 4, where future perspectives are outlined, we discuss how to obtain T_B and ΔT self-consistently as a function of time throughout the solidification process.

Since the chamber's characteristic spatial size lies in the interval of 10^1 to 10^4 meters, the effect of pressure is of little importance here so the convective bulk can be assumed to be isoviscous. Our model focuses predominantly on tank-like chambers, but since the model is developed in one dimension (1D), it can be applied also to systems with a large aspect ratio such as sills.

The key quantity that enters the crystal settling dynamics is the characteristic velocity of the convective flow. We will employ Grossman-Lohse theory (i.e., scaling laws for Nusselt and Reynolds numbers) after Ahlers et al. [2009], who summarize results of both theoretical and experimental works for the isoviscous Rayleigh-Bénard convection. Ahlers studies the $Pr \times Ra$ model space and distinguishes between two kinetic- and thermal-energy dissipation modes dominated either by the boundary layer region or the interior bulk region. In a system with Prandtl number greater than unity ($Pr > 1$), always satisfied in our application, the thermal boundary layer is thinner than the viscous boundary layer. For the intended range of Prandtl and Rayleigh numbers (i.e., $Pr \in [10^3 - 10^5]$, Ra unconstrained), we will always find ourselves in the the regime dominated by the bulk energy dissipation with thin thermal boundary layer nested in the viscous boundary layer. The scaling laws for this setup read

$$Re(Ra, Pr) \sim Ra^{4/9} Pr^{-2/3}\,, \tag{1.3}$$

$$Nu(Ra, Pr) \sim Ra^{1/3}\,, \tag{1.4}$$

where the Reynolds number $Re(Ra, Pr)$ is defined by the volume-averaged root mean square velocity W_{rms}. Recalling the traditional definition of the Reynolds number gives

$$W_{\mathrm{rms}}(Ra, Pr) = \frac{\nu Re(Ra, Pr)}{H_0 - h}\,. \tag{1.5}$$

By invoking the definition of the Nusselt number and Fourier's law of heat conduction,

$$Nu = \frac{\mathcal{F}}{k\Delta T/(H_0 - h)}\,, \tag{1.6}$$

$$\mathcal{F} \sim k\Delta T/h_b\,, \tag{1.7}$$

where k is the thermal conductivity of magma, h_b the thermal boundary layer thickness, and $\mathcal{F}$ the heat flux through the roof, one obtains the thermal boundary layer thickness from the scaling law Eq. (1.4):

$$h_{\mathrm{b}} \sim Ra^{-1/3}(H_0 - h)\,. \tag{1.8}$$

The reader should note that the thermal boundary layer thickness does not scale with the remaining height of the chamber, $H_0 - h$.

1.1 Thermal boundary layer

1.1.1 Geometry, nucleation and growth

While the thermal boundary layer (TBL) is assumed to be a non-deforming fluid layer through which all crystals fall via classic Stokes sinking, the settling dynamics in the convective bulk are more complicated. The following section deals with processes in the TBL. Nucleation of crystals is controlled by the nucleation delay, a temperature drop below the liquidus that is necessary for crystallization to occur. Since the temperature gradient is confined to the thermal boundary layer, nucleation will commence in this region and the segment of the boundary

layer with sufficient undercooling shall be, henceforth, termed the nucleation sublayer (see Fig. 1.1). Both crystal nucleation and growth are thermally activated processes. Their rates, $\mathcal{G}$ and $\mathcal{N}$, are temperature dependent and thus vary across the TBL. The thickness of the boundary layer can be calculated as

$$h_{\mathrm{b}} = (Ra_{\mathrm{cr}}/Ra)^{-1/3}\,(H_0 - h)\,, \tag{1.9}$$

where Ra_{cr} is the critical Reyleigh number necessary for the onset of thermal convection (typically, $Ra_{\mathrm{cr}} \sim \mathcal{O}(10^3)$, but the exact value depends on the geometry of the system and imposed boundary conditions). We assume a constant temperature gradient in the thermal boundary layer, which allows us to write the temperature profile as

$$T(z) = (T_B - T_R)\frac{z}{h_b} + T_R\,, \tag{1.10}$$

which immediately implies that the thickness of the nucleation sublayer, h_n, is given by

$$h_n = \begin{cases} h_b & T_B \leq T_L - \varepsilon\,, \\ h_b(T_{\mathrm{L}} - \varepsilon - T_R)/(T_{\mathrm{B}} - T_R) & \text{otherwise}\,, \end{cases} \tag{1.11}$$

where T_L denotes the liquidus temperature.

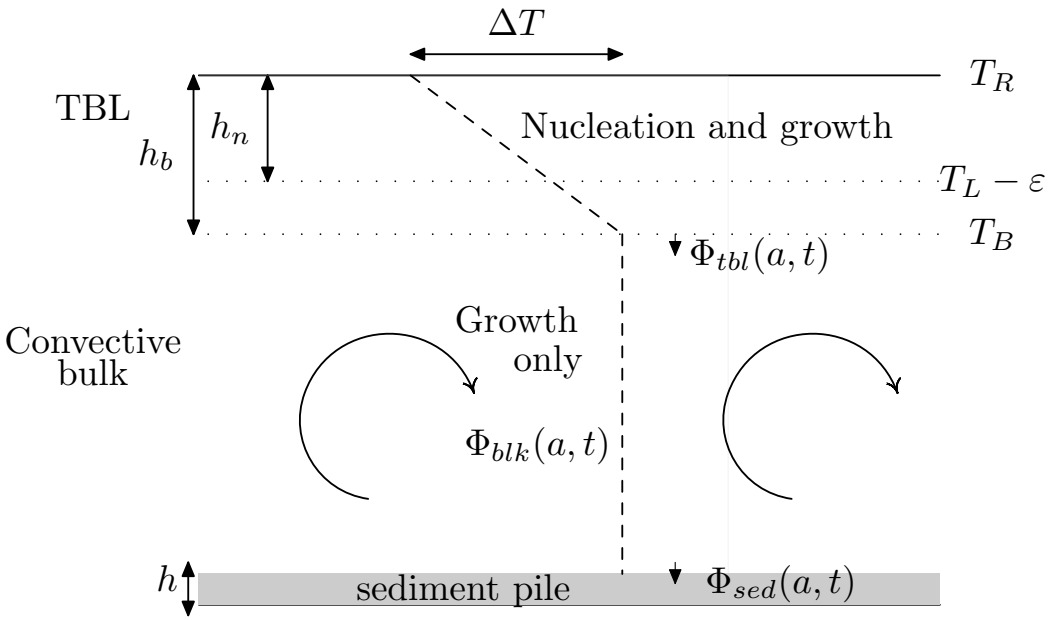

Figure 1.1: Sketch of a magma chamber with delineated temperature profile (dashed line), marked spatial dimensions, and corresponding temperatures (the sketch is not to scale, and the profile is smooth in the TBL/bulk transition area). Crystal size distribution $\Phi_{\mathrm{tbl}}(a)$ falls into the (convecting) bulk, where their population is described by $\Phi_{\mathrm{blk}}(a)$, and crystals eventually settle at the base of the chamber with their size distribution given by $\Phi_{\mathrm{sed}}(a)$ and gradually form a sediment pile with increasing height h.

Crystals are extracted from the layer by gravitational settling - a spherical crystal with radius a falls through the layer with the Stokes settling velocity given by

$$W_S(a) = \frac{2g_0\Delta\rho}{9\rho_F\nu}a^2\,, \tag{1.12}$$

where ρ_F is the density of the liquid magma and $\Delta\rho = \rho_C - \rho_F$ denotes the density contrast between crystals and magma (ρ_C is the density of the solid phase). Now, let us conduct a simple analysis to estimate the characteristic residence time scale t_b for crystals in the boundary layer. As a crystal progresses through the fluid layer, it grows in size at the rate of $\mathcal{G}(T)$ and it will attain radius $a_b \approx \tilde{\mathcal{G}} t_b$ upon its extraction, where $\tilde{\mathcal{G}}$ denotes the averaged growth rate across the boundary. The corresponding average Stokes settling velocity over the boundary segment then reads

$$\overline{W}_S \approx \frac{1}{a_b}\int_0^{a_b} \frac{2g_0\Delta\rho}{9\rho_F\nu} a^2 \mathrm{d}a = \frac{2g_0\Delta\rho}{27\rho_F\nu}\tilde{\mathcal{G}}^2 t_b^2 \,, \tag{1.13}$$

$$t_b \approx h_b/\overline{W}_S \,, \tag{1.14}$$

which implies the residence time of crystals in the boundary layer is of the order of

$$t_b \sim \left(27\nu h_b \rho_F / 2g_0\Delta\rho\tilde{\mathcal{G}}^2\right)^{1/3} \,. \tag{1.15}$$

This time scale can be later used to estimate the size of the time step in the numerical code. The nucleation process in the boundary layer is continuous - crystals are nucleated, they grow in size, and eventually fall into the convecting bulk. This prompts us to introduce a crystal size distribution function for extracted crystals $\Phi_{\mathrm{tbl}}(a,t)$, which gives us the number of crystals with radius between a and $a+\mathrm{d}a$ at time t per unit volume as $\Phi_{\mathrm{tbl}}(a,t)\mathrm{d}a$. We will demonstrate later that this distribution quickly saturates and is no longer time-dependent (it reaches the steady state).

1.2 Bulk processes and crystal settling

Now, let us shift our attention to the bulk and processes operating therein. We employ the assumption of a dilute suspension (a premise we can easily check at any time during the simulation) so any crystal-driven convection is omitted. In accordance with the definition of $\Phi_{\mathrm{tbl}}(a,t)$, we can analogously introduce crystal size distributions for crystals in suspension $\Phi_{\mathrm{blk}}(a,t)$ and the sedimented crystals $\Phi_{\mathrm{sed}}(a,t)$. The fate of each crystal in the bulk is determined by its Stokes' settling velocity (and thus its radius) in comparison to the background flow velocity. If $W_S \ll W_{\mathrm{rms}}$ holds (limit of tiny crystals in vigorously convecting fluid), the crystal gets swept by the convective flows and essentially becomes a passive tracer of the fluid movement. The convection in magma chambers is generally assumed to be turbulent, and therefore, we employ a simplification that the crystals are distributed in the suspension uniformly. As mentioned in the introduction, this end-member was investigated by Martin and Nokes who experimentally (Martin and Nokes [1988]) and theoretically (Martin and Nokes [1989]) derived the following exponential settling law

$$\frac{\mathrm{d}K(t)}{\mathrm{d}t} = -AW_S C_{\mathrm{bot}} \,, \tag{1.16}$$

where A is the base area of the chamber, $K(t)$ is the time-varying crystal population (for the definition of a crystal population, see Chapter 2), and C_{bot} is the volumetric concentration of crystals at the bottom of the chamber. For crystals

uniformly distributed throughout the convective bulk, the concentration simply follows

$$C_{\mathrm{bot}}(t) = \frac{K(t)}{A(H_0 - h)}\,. \tag{1.17}$$

The interpretation of this mode is as follows: Whenever a crystal happens to be transported close to the base of the chamber, the likelihood of its settling is directly proportional to the particle Stokes' velocity, because the convective velocity tends to zero at the boundary and the crystals can separate from the liquid in the near-boundary layer.

On the contrary, if $W_S \gg W_{\mathrm{rms}}$ holds (the limit of nearly static magma), the fluid appears nearly motionless to the crystals and they continue in gravitational settling. We will follow Patočka et al. [2022], who propose the implementation of the shrinking velocity, v_{sh}, that describes how the volume with $K(t)$ encased particles decreases with time. This leads to a modification for the expression of the crystal concentration at the bottom of the chamber to

$$C_{\mathrm{bot}}(t) = \frac{K(t)}{A(H_0 - h - v_{\mathrm{sh}}t)}\,. \tag{1.18}$$

Evidently, sedimentation becomes more effective with increasing shrinking velocity. Integration of Eq. (1.16) upon inserting Eq. (1.18) gives a compact analytical formula,

$$K(t) = K_0 \left(1 - \frac{t v_{\mathrm{sh}}}{H_0 - h}\right)^{\frac{W_S}{v_{\mathrm{sh}}}}\,. \tag{1.19}$$

with v_{sh} defined by

$$v_{\mathrm{vsh}} = \begin{cases} W_S - \gamma W_{\mathrm{rms}} & \text{if } W_S > \gamma W_{\mathrm{rms}}\,, \\ 0 & \text{if } W_S \leq \gamma W_{\mathrm{rms}}\,, \end{cases} \tag{1.20}$$

where $\gamma = 0.7$ (Patočka et al. [2022]). Martin and Nokes reported that their settling law exhibits a discrepancy of only 20% for $W_S/W_{\mathrm{rms}} \approx 0.5$. For the sake of simplicy, we adhere to using $\gamma = 1$ in Chapter 3. In the limit of a gravitationally settling crystal in static fluid, the shrinking velocity follows $v_{\mathrm{sh}} \longrightarrow W_S$, on the contrary, the shrinking velocity tends to zero for a crystal with negligible size, thus $v_{\mathrm{sh}} \longrightarrow 0$. Two limiting cases of Eq. (1.19) yield

$$K_0 \left(1 - \frac{t v_{\mathrm{sh}}}{H_0 - h}\right)^{\frac{W_S}{v_{\mathrm{sh}}}} = \begin{cases} K_0 \exp\left(\frac{-W_S t}{H_0 - h}\right) & v_{\mathrm{sh}} \longrightarrow 0\,, \\ K_0 \left(1 - \frac{W_S t}{H_0 - h}\right) & v_{\mathrm{sh}} \longrightarrow W_S\,. \end{cases} \tag{1.21}$$

Following Patočka et al. [2022], we shall address these two end-members respectively as dust-like and stone-like regimes. The concept of shrinking velocity can be easily visualized as the advance of a sedimentary front, see Fig. 1.2 below.

The system of equations Eq. (1.16)–Eq. (1.19) was solved in Patočka et al. [2022] for olivine crystal cargo, i.e., for a set of crystals of with predefined radii, injected uniformly into the convective bulk. Here, the model is expanded to crystals that self-consistently nucleate and grow within the chamber. Eq. (1.16) is modified to account for the influx of crystals from the TBL, and the shrinking velocity of each crystal population evolves with time, since $W_S \propto a^2$ and $a(t) =$

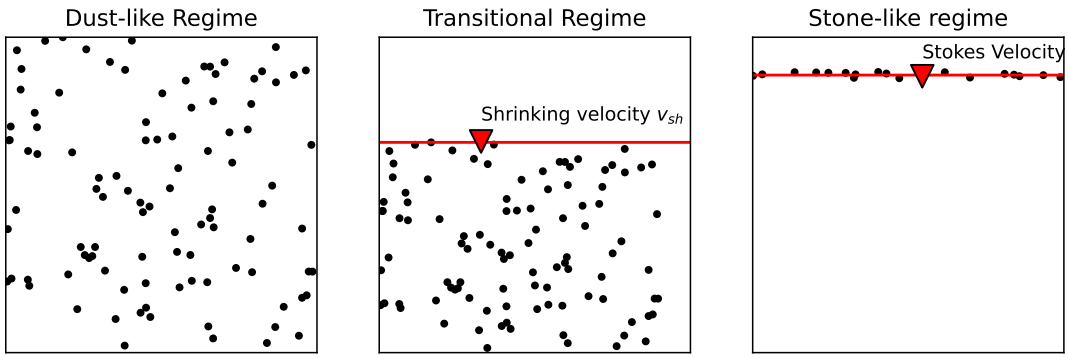

Figure 1.2: Visualization of individual regimes - pure dust-like regime (panel 1), transitional regime via the concept of the shrinking velocity (red line, panel 2), and pure stone-like regime, i.e., limit $v_{\mathrm{sh}} \longrightarrow W_S$ (red line, panel 3).

$a_0 + \mathcal{G}(T_B)t$, where a_0 is the radius to which the crystal has grown in the TBL. The governing equation for the coupled model of crystal sedimentation and continuous influx of crystals can be written as

$$\frac{\mathrm{d}\Phi_{\mathrm{sed}}(a,t)}{\mathrm{d}t} = -AW_S(a)C_{\mathrm{bot}} + \Phi_{\mathrm{tbl}}(a)\,, \tag{1.22}$$

where C_{bot} reflects the volume, in which crystals of each family are mixed effectively. This volume intrinsically depends on the radius of the family, hence, C_{bot} depends on the bulk distribution $\Phi_{\mathrm{blk}}(a,t)$. Unless the fluid conditions change, we can expect a steady state to arise, in which the bulk and sediment crystal size distribution become time-independent again (the validity of this assumption will be discussed later). Naturally, crystals can (and under certain conditions, we expect them to) undergo smooth transition from one end-member described in Eq. (1.21) to the other.

Once we calculate the steady state distributions $\Phi_{\mathrm{sed}}(a)$ and $\Phi_{\mathrm{blk}}(a)$, the crystal fraction in the bulk, ϕ, (auxiliary quantity so we can check the assumption of a dilute suspension is satisfied, $\phi \ll 1$), and the mean crystal radius in the sediment, $\bar{a}_d$, can be evaluated as

$$\phi = \frac{4\pi}{3(H_0 - h)} \int_0^{a_{\max}} a^3 \Phi_{\mathrm{blk}}(a)\mathrm{d}a\,, \tag{1.23}$$

$$\bar{a}_d = \int_0^{a_{\max}} a\Phi_{\mathrm{sed}}(a)\mathrm{d}a \Big/ \int_0^{a_{\max}} \Phi_{\mathrm{sed}}(a)\mathrm{d}a\,, \tag{1.24}$$

where $a_{\max}$ denotes the maximum radius contained in the distribution.

1.2.1 Single zero-sized crystal population

It is instructive to first perform an exercise in which a population of K_0 crystals with a negligible initial radius ($a_0 = 0$, for simplicity) is suspended in the bulk, and settles in accord with the dust-like end-member regime. Crystals grow at a constant rate $\mathcal{G}_0$ and they reach radius $a = \mathcal{G}_0 t$ at time t. The number of crystals

follows

$$\frac{\mathrm{d}K(t)}{\mathrm{d}t} = -\frac{\lambda \mathcal{G}_0^2 t^2}{H_0 - h} K(t)\,, \tag{1.25}$$

$$K(t) = K_0 \exp\left(-\frac{\lambda \mathcal{G}_0^2 t^3}{3(H_0 - h)}\right)\,, \tag{1.26}$$

where $\lambda = 2g_0\Delta\rho/9\rho_F\nu$ is the constant of proportionality from the Stokes formula. Because time and crystal radius are uniquely related in this exercise, $a = \mathcal{G}_0 t$, we can express how the population decreases as the crystal radius increases,

$$K(a) = K_0 \exp\left(-\frac{\lambda a^3}{3\mathcal{G}_0(H_0 - h)}\right)\,. \tag{1.27}$$

Any change in the number of suspended crystals results in sediment formation. Hence, the crystal size distribution of the sediment, $\Phi_{\mathrm{sed}}(a)$, is given as $\mathrm{d}K = \Phi_{\mathrm{sed}}(a)\mathrm{d}a$ and can be obtained by taking the derivative of Eq. (1.25),

$$\Phi_{\mathrm{sed}}(a) = \frac{\mathrm{d}K}{\mathrm{d}a} = \frac{3K_0 a^2}{(H_0 - h)\mathcal{G}_0} \exp\left(-\frac{\lambda a^3}{3\mathcal{G}_0(H_0 - h)}\right)\,. \tag{1.28}$$

Altogether, we expect the distribution functions to scale as

$$\Phi_{\mathrm{sed}}(a) \sim a^2 \exp\left(-a^3\right)\,, \tag{1.29}$$

$$K(a) \sim \exp\left(-a^3\right)\,. \tag{1.30}$$

This quick analysis predicts a result equivalent (in terms of a scaling) to the one reported by Jarvis and Woods [1994], who completely neglect dynamics in the TBL and work with the zero initial radius approximation. A question arises as to whether how the predicted size distribution Φ_{sed} modifies when an influx of crystals from TBL continuously re-populates the bulk. In Chapter 3, we will compare these scalings with results predicted by the full model.

1.3 Nucleation and growth laws

For the purpose of comparison with previous work and in order to familiarize ourselves with the basic features of crystallization kinetics, we first employ the relationships from Jarvis and Woods [1994]. In their work, the crystal growth and nucleation rate are given as:

$$\mathcal{G}_{\mathrm{pow}}(T) = \frac{\mathrm{d}a}{\mathrm{d}t} = V_{\mathrm{pow}} \left(\frac{T_{\mathrm{L}} - T}{T_{\mathrm{L}} - T_{\mathrm{r}}}\right)^p\,, \tag{1.31}$$

$$\mathcal{K}_{\mathrm{pow}}(T) = \frac{\mathrm{d}K}{\mathrm{d}t} = N_{\mathrm{pow}} \left(\frac{T_{\mathrm{L}} - \varepsilon - T}{T_{\mathrm{L}} - \varepsilon - T_{\mathrm{r}}}\right)^q\,, \tag{1.32}$$

where V_{pow} and N_{pow} are the reference growth and nucleation constants, respectively. Moreover, for the sake of simplicity we will restrict ourselves to using only $p = q = 1$ (linear laws). Subsequently, we will replace these laws by a more realistic model by Hort [1997], the model (henceforth termed the Hortian curves) is based on a simplified physico-chemical foundation (for details, see Hort [1997],

Dowty [1980] and Spohn et al. [1988]) and predicts the nucleation and growth rate depending solely on the temperature in the form of bell-shaped curves (i.e., with decreasing temperature T, the rates first increase, but then decrease again, following a long attenuation tail). The mathematical form of the nucleation rate automatically predicts a certain nucleation lag while the onset of the growth rate occurs immediately at the liquidus temperature. Both rates have a maximum and then they plummet rapidly for high undercoolings. The adopted crystal growth rate and the nucleation rate are given by

$$\mathcal{G}_{\mathrm{Hort}}(T) = G_0 \left(\frac{T_{\mathrm{G}}^*(T_{\mathrm{L}} - T)}{T(1 - T_{\mathrm{G}^*})} \right) \exp\left(-\frac{T_{\mathrm{L}} \left(T_{\mathrm{G}^*} - \frac{T}{T_{\mathrm{L}}} \right)}{T(1 - T_{\mathrm{G}^*})} \right) , \tag{1.33}$$

$$\mathcal{K}_{\mathrm{Hort}}(T) = K_0 \exp\left(\frac{T_{\mathrm{G}^*}}{1 - T_{\mathrm{G}^*}} \left(\frac{T - T_{\mathrm{L}} T_{\mathrm{I}}^*}{T_{\mathrm{I}}^* T} - \frac{(1 - T_{\mathrm{I}}^*)^3}{1 - 3T_{\mathrm{I}^*}} \right.\right. \tag{1.34}$$

$$\left.\left. \times \left(\frac{1}{T_{\mathrm{I}^*}(1 - T_{\mathrm{I}^*})^2} - \frac{T_{\mathrm{L}}}{T\left(1 - \frac{T}{T_{\mathrm{L}}}\right)^2} \right) \right) \right) ,$$

where G_0 and K_0 are amplitudes of the crystal growth rate and nucleation rate, respectively. The characteristic shape of Hortian curves is displayed in Fig. 1.3.

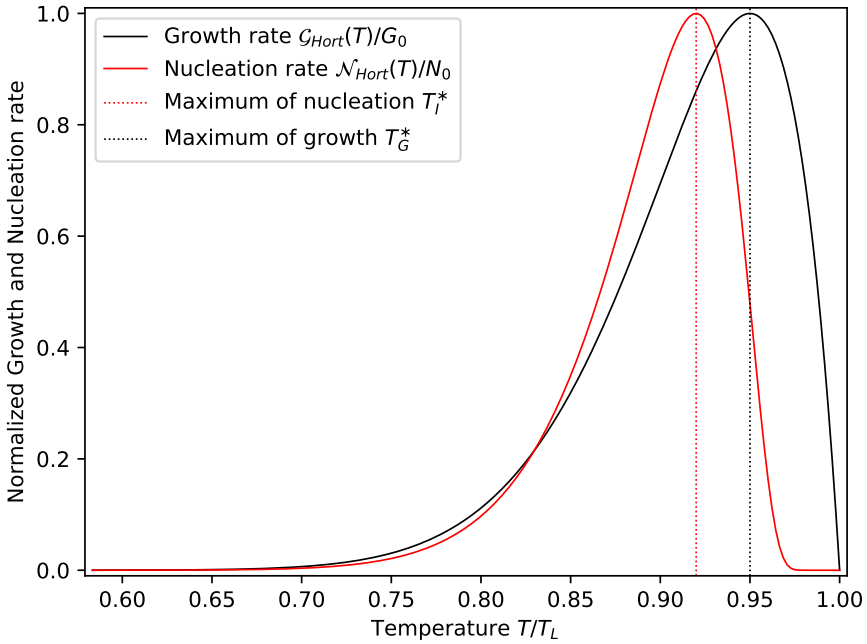

Figure 1.3: Hortian curves for $T_G^* = 0.95$ and $T_I^* = 0.92$ - crystal nucleation (red) and crystal growth (black) rates as functions of temperature after Eq. (1.33) and Eq. (1.34) norma. The temperature axis normalized by the liquidus temperature.

Temperatures T_{I}^* and T_{G}^* denote the normalized values of temperature, at which maxima of each rate occurs, defined as

$$T_{\mathrm{I}}^* := \frac{T_{\mathrm{I,max}}}{T_{\mathrm{L}}} , \quad T_{\mathrm{G}}^* := \frac{T_{\mathrm{G,max}}}{T_{\mathrm{L}}} . \tag{1.35}$$

where $T_{\mathrm{I,max}}$ and $T_{\mathrm{I,max}}$ are the dimensional values at which the nucleation and growth activities peak. Note that the nucleation lag ε does not enter the Hortian kinetic equations per se. Nucleation lag is an intrinsic consequence of the equation and its value thus scales with the normalized temperature of the maximum nucleation rate (technically, the nucleation rate is always non-zero, it just becomes negligible close to the liquidus temeprature). Throughout the thesis, we consider the nucleation in the TBL to be heterogeneous, however, manipulation with the kinetic law parameters allows us to reach arbitrarily low nucleation lags, thereby simulating the homogeneous nucleation.

1.4 Time scales and quasi-steady approach

At first glance, coupling the processes of chamber cooling with the temperature dependent nucleation and growth kinetics, together with the settling dynamics and sediment formation, looks complicated. However, the model simplifies greatly if we look at the typical time scales of the individual processes, which allows us to isolate them and treat them individually. We already estimated the residence time scale in the boundary layer, t_b (see Eq. (1.15)). Furthermore, Eq. (1.26) gives the characteristic residence time scale for dust-like particles (stone-like particles differ in a constant of proportionality) in the bulk as

$$t_{\mathrm{res}} \sim \left(3\rho_F \nu (H_0 - h)/g_0 \Delta\rho \mathcal{G}^2\right)^{1/3} . \tag{1.36}$$

Earlier, we postulated that after a transient phase that is needed to fill the TBL and the convective bulk with crystals, the crystal size distributions equilibrate and reach a steady state. When crystals first nucleate in the TBL, it takes time t_s^{tbl} to reach the steady state, at which the crystal distribution $\Phi_{\mathrm{tbl}}(a,t)$ is no longer time-dependent, and analogously, we introduce the time t_s^{blk} after which $\Phi_{\mathrm{sed}}(a,t)$ and $\Phi_{\mathrm{blk}}(a,t)$ become steady. These time scales are linked to the residence time scales as $t_s^{\mathrm{tbl}} \gtrsim t_b$ and $t_s^{\mathrm{blk}} \gtrsim t_{\mathrm{res}}$. The above estimates address the dynamics of crystal populations that form in a chamber with a given temperature profile. The estimate for the convective time cooling scale, i.e. for the time evolution of the temperature profile within the chamber, comes from the energy balance (see Eq. (4.8)):

$$t_c \sim (H_0 - h)\rho_F c_p (T_B - T_R)/\mathcal{F} . \tag{1.37}$$

Therefore, all temperature-dependent quantities vary over time scale $\sim \mathcal{O}(t_c)$. Provided that $t_c \gg t_s^{\mathrm{blk}}$, all time- and temperature-dependent parameters (roof and bulk temperatures T_R and T_B, growth rate $\mathcal{G}$) vary negligibly over times $\sim \mathcal{O}(t_s^{\mathrm{blk}})$. In comparison, the time necessary for the onset of the steady state in the TBL is ephemeral. This is to be termed the quasi-steady approach and it represents a key assumption for this thesis. Yet another integral consequence of this approach is a balance between the production rate by crystallization (i.e., the number of crystals nucleated in the thermal boundary layer per time unit) and the sedimentation rate (i.e., the number of crystals leaving the suspension per time unit): In the steady state, the flux of crystals falling into the bulk from TBL must even out the flux of crystals from the bulk into the sediment. When the temperature conditions change, the steady state distribution will reflect the change with a response time that is expected to be $\sim \mathcal{O}(t_s^{\mathrm{blk}})$ at most.

1.5 Onset of solidification

Right after the magma emplacement, heat flux through the roof is significant and the fluid cools rapidly. Naturally, if any crystals (nucleated in the boundary layer, or injected as cargo) were to find their way to the convecting bulk whilst it is still superheated (i.e., $T_B > T_L$), they would start remelting. We omit this stage of cooling and always set the bulk temperature to $T_B \leq T_L$.

Solidification of the body is hindered either by the nucleation or by the growth process, and it is the value of the nucleation lag that determines which is the case. With regard to ΔT, we must distinguish two cases, i) $\Delta T < \varepsilon$ and ii) $\Delta T \geq \varepsilon$, the respective onset of solidification is depicted in Fig. 1.4. In the first case, the roof temperature is exactly at the nucleation threshold and the nucleation in the TBL occurs with the slightest shift below this temperature. In the latter, the bulk temperature is exactly at the liquidus, the slightest shift above this temperature would result in crystals remelting in the bulk.

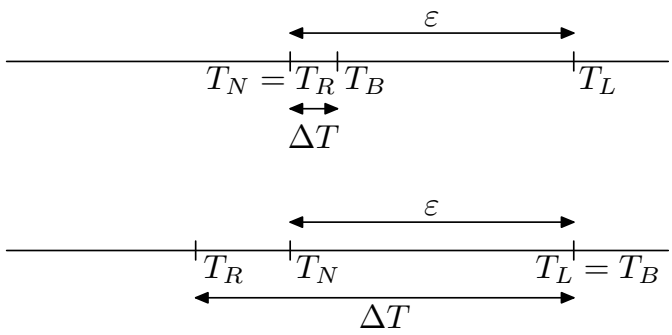

Figure 1.4: Two initial conditions: i) $\Delta T < \varepsilon$ (top image), the nucleation commences as soon as the roof temperature drops down to nucleation temperature $T_N = T_L - \varepsilon$, ii) $\Delta T \geq \varepsilon$ (bottom image), the nucleation starts the moment the bulk temperature drops down to T_L.

When $\Delta T > \varepsilon$ holds, the nucleation commences right off the bat in the TBL. On the contrary, for large nucleation lags (exceeding the temperature contrast ΔT), the initial undercooling in the TBL is insufficient for the solidification to start. Later in Section 3.3, where a parametric study is performed, we refer to the two possible scenarios from Fig. 1.4, because they provide a constraint on the meaningful choices on T_B and ΔT.

2. Numerical implementation

To solve the governing equations, we developed a numerical code `1DNGMC`, written in *Python3* (see Attachment). While *Python3* is not an ideal language for computationally demanding simulations, such as when 2D or 3D partial differential equations are solved, the problem at hand is of statistical nature – we chose *Python3* to utilize its perks in the domain of data storage and data manipulation. This section describes our numerical implementation of the crystal size distribution computation.

2.1 Boundary layer processes

The nucleation sub-layer (which comprises a fraction of or the whole thermal boundary layer) is split into $N-1$ layers by N interfaces discretized evenly by spatial step Δh. Within each layer, nucleation occurs with a uniform probability density μ_i, see Fig. 2.1 for details. Processes within the boundary layer operate on a time scale t_b (see Eq. (1.15)), thus, the time step Δt_b can be taken as a sufficiently small fraction of this estimate. At each time step, $N-1$ families of crystals are born, one in each layer (a "generation of families"). The $j-$th crystal family ($1 \leq j \leq N-1$) is nucleated at the depth z_j^0 with a population of $K = \mathcal{N}(T_j^0)\Delta z \Delta t_b$ crystals (the temperature T_j^0 corresponds to z_j^0). The crystal radius – same for each crystal family – increases by $\Delta a = \mathcal{G}(T_j)\Delta t_b$, where T_j corresponds to the current depth coordinate z_j of the family, and sinks a depth of $\Delta z = W_S(a_j)\Delta t_b$. Note that, the number of crystals K is treated as a real number (not integer), and that the radius upon nucleation is zero.

To compute the size distribution of crystals falling into the bulk from the TBL, Φ_{tbl}, two methods were implemented, coined as the 0-generation and step-by-step methods, respectively. The latter method advances in time just as a natural system is expected to: each time step, a generation of new families are born, and all the crystals from older families are inflated in size by Δa and transported down by Δz. Crystals that have reached the base of TBL then form the desired $\Phi_{tbl}(a,t)$ distribution.

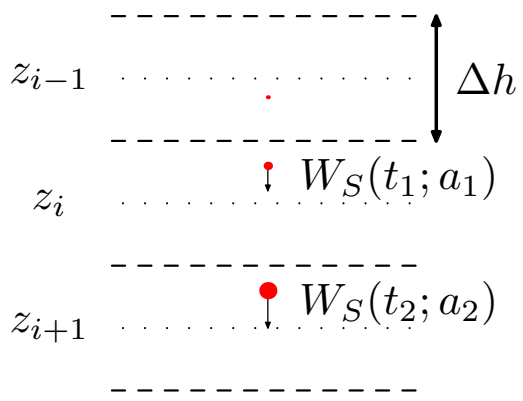

Figure 2.1: Evolution of a crystal family (red dot) in the thermal boundary layer.

After a transient period, we expect a steady state situation to arise, in which the number of crystals nucleated per time step in the boundary layer balances the crystal flux into the convecting bulk - the step-by-step method was used to confirm this expectation and to evaluate the transient time. The 0-generation method benefits from the observation that in the steady-state, $\Phi_{tbl}(a)$ is identical to the size distribution of crystals from a single generation, when only the final radius a of each family is recorded. Therefore, we only have to nucleate one generation of families and make them all sink through the entire TBL to obtain the steady state distribution. Since both methods yield the same results, we later adhere to the computationally faster 0-generetaion method.

The reader should also take note that in cases where the nucleation sublayer makes up only a portion of the boundary layer, nucleation does not happen elsewhere in the layer. Nevertheless, crystals do naturally continue to grow there. All of the $N-1$ crystal families are subsequently sorted into a discrete histogram with n_b bins ($N > n_b$), each bin represented by mean radius (it is advised to superpose the process for $n_g \sim \mathcal{O}(10)$ generations to reach a sufficiently smooth final distribution, alternatively, we can drastically increase N). Following the notation from the previous chapter, we denote the steady state crystal distribution $\Phi_{\mathrm{tbl}}(a)$.

2.2 Bulk processes

Processes inside the bulk operate on a much longer time scale. In accord with Section 1.4, we can estimate the appropriate time step for this phase, Δt_s, as a sufficient small fraction of Eq. (1.36) ($\Delta t_s \gg \Delta t_b$). Consequently, the distribution falling into the convective bulk at each time step Δt_s is simply given as $\Phi_{\mathrm{tbl}}(a)\Delta t_s/\Delta t_b$ (the TBL distribution is normalized by the total number of crystals here). Generally, the bulk temperature T_B is below the liquidus temperature, and so the crystals in each family grow in size and some of them are lost to the sediment at each time step. We have implemented two ways of handling the sedimentation process, i) method, in which one only works with discrete histograms representing $\Phi_{\mathrm{blk}}(a,t)$ and $\Phi_{\mathrm{sed}}(a,t)$, without storing any information about the individual crystal families that form these distribution (this method requires very little CPU memory), and ii) method, in which all individual crystal families are traced (computationally more demanding, but allowing us to handle more complex settling dynamics, as described below).

The first method, termed the method of distributions, is straightforward in nature as all we need to do is to pour crystals into corresponding bins whilst gradually changing the bin size of the bulk and sedimentation histograms, as the largest obtained radius a_{max} evolves with time (for a fixed number of bins, n_b, the bin size is a_{max}/n_b). The method is outlined below in Fig. 2.2. The sedimentation loop either runs with a fixed number of time steps or we can stop it the moment a steady state is reached (i.e., the influx of crystals is compensated by the sedimentation process and distributions $\Phi_{\mathrm{blk}}(a,t)$ and $\Phi_{\mathrm{sed}}(a,t)$ no longer evolve in time).

We assume that, within each bin, the crystal sizes are distributed uniformly. During each time step, we pour distribution $\Phi_{\mathrm{tbl}}(a)\Delta t_s/\Delta t_b$ into the bulk distribution, and let the crystals settle by applying Eq. (1.16). If the number of

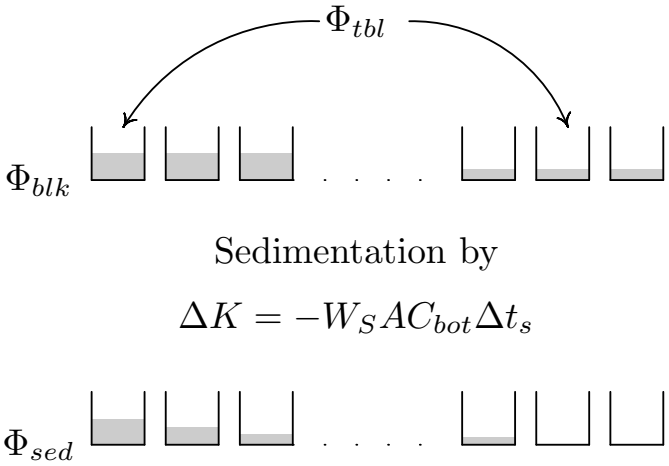

Figure 2.2: Visualisation of the method of distributions at an early phase of the sedimentation loop - pouring $\Phi_{\mathrm{tbl}}(a)$ into histogram bins. While TBL bins remain constant, bulk and sedimentation bins (displayed above) gradually increase and they are of the same size.

crystals in the last bin is non-negligible, we extend $a_{\max}$ and hence the the size of the bins, and reshuffle crystals from the antecedent bins into the new ones. Implementing the crystal pouring for gradually changing bin size is a bit tricky, but overall this method is advantageous when we are only interested in dust-like sedimentation.

When applying Eq. (1.16), i.e. the sedimentation law, the quantity of key interest is the concentration of crystals near the base of the liquid magma, C_{bot}. It is this quantity that captures the mixing and settling of crystals in the bulk described in Section 1.2. Problem of the method of distributions is that it does not keep track of the volume in which a family of crystals is contained. When a family falls into the bulk, the volume in which it is effectively mixed shrinks with time. To compute this volume, one must know when the family has fallen into the bulk, but such an information is lost in the method of distributions. Moreover, this method offers no way of introducing, e.g., depth-dependent growth laws, making it less attractive for future development of our numerical tool.

On the contrary, the tracing method requires a lot of CPU memory and seems complicated. We can, however, simplify it by realizing another consequence of the quasi-steady approach: any two distributions that had fallen into the convecting bulk within the same sedimentation loop follow the same evolutionary path. The tracing method is outlined below, we follow the history of a distribution $\Phi_{\mathrm{tbl}}(a)\Delta t_s/\Delta t_b$ (marked in red) until it completely settles down. At the $i-$th time step, each family splits into $\bar{\Phi}_{\mathrm{tbl},(i)} = \bar{\Phi}_{\mathrm{tbl},(i+1)} + \tilde{\Phi}_{\mathrm{tbl},(i+1)}$ (tilde denotes settled crystals, bar then its complement remaining in the bulk, the lower index denotes the number of time steps the distribution had spent in the bulk so far). Naturally, it will take L steps (we do not know this number apriori) for all families to settle completely (since we are working with non-integer numbers of crystals, we have to impose an approprite cut-off, typically one/few tenths of a crystal), increasing the fixed number of time steps M (we set M high enough so that $M \gg L$ always holds) increases the accuracy. By keeping track of the individual crystal families, we are provided with a way of introducing the con-

cept of the shrinking velocity as well as purely stone-like particles into the model (cf. Fig. 1.2).

$$
\begin{aligned}
1 \times \Delta t_s : \Phi_{\text{blk (start)}} &= \left[\Phi_{\text{tbl}}\right] \\
\Phi_{\text{sed}} &= \left[\tilde{\Phi}_{\text{tbl}}\right] \\
\Phi_{\text{blk (end)}} &= \left[\bar{\Phi}_{\text{tbl}}\right] \\
2 \times \Delta t_s : \Phi_{\text{blk (start)}} &= \left[\Phi_{\text{tbl}}, \bar{\Phi}_{\text{tbl,(1)}}\right] \\
\Phi_{\text{sed}} &= \left[\tilde{\Phi}_{\text{tbl}}, \tilde{\Phi}_{\text{tbl,(1)}}\right] \\
\Phi_{\text{blk (end)}} &= \left[\bar{\Phi}_{\text{tbl}}, \bar{\Phi}_{\text{tbl,(2)}}\right] \\
\vdots \qquad\quad \vdots &\qquad\quad \vdots \\
\vdots \qquad\quad \vdots &\qquad\quad \vdots \\
L \times \Delta t_s : \Phi_{\text{blk (start)}} &= \left[\Phi_{\text{tbl}}, \bar{\Phi}_{\text{tbl,(1)}}, \ldots, \bar{\Phi}_{\text{tbl,}(L-1)}\right] \\
\Phi_{\text{sed}} &= \left[M\tilde{\Phi}_{\text{tbl}}, (M-1)\tilde{\Phi}_{\text{tbl,(1)}}, \ldots, (M-L+1)\tilde{\Phi}_{\text{tbl,}(L-1)}\right] \\
\Phi_{\text{blk (end)}} &= \left[\bar{\Phi}_{\text{tbl}}, \bar{\Phi}_{\text{tbl,(1)}}, \ldots, \bar{\Phi}_{\text{tbl,}(L)}\right]
\end{aligned}
$$

To mimic the transition between dust-like and stone-like particles, the shrinking velocity v_{sh} described in Section 1.2 is implemented. We recall that v_{sh} captures the behaviour of the settling front once a population of crystals falls into the bulk, i.e. it allows one to assess C_{bot}. We assume that each crystal family follows the exponential settling law until its radius exceeds the transition radius,

$$a_{\text{tr}} = (9W_{\text{rms}}\gamma\rho_F\nu/2g_0\Delta\rho)^{1/2} \ . \tag{2.1}$$

for which the Stokes velocity of crystals becomes comparable to the mean velocity of the background flow, $W_S = \gamma W_{rms}$. Upon reaching the transition radius, the crystal family starts to settle down with gradually changing particle concentration given by Eq. (1.18), in which the shrinking velocity v_{sh} continuously evolves with time. In addition, if a crystal happens to already have a radius larger than this transient one upon entering the bulk, it will simply continue in the Stokesian fall, this time across the entire height of the chamber, $H_0 - h$.

In Chapter 3, we will sometimes make references to individual regimes: pure dust-like regime simply means that crystals settle according to the Martin and Nokes sedimentation law. Stone/dust transition then refers to the situation discussed above, i.e., $W_S = \gamma W_{\text{rms}}$ is satisfied at some point of the crystal family's history. Pure stone-like regime then refers to particles that spend their whole life in the Stokesian fall. In our code, the pure dust-like regime is the default mechanism of sedimentation. Both stone/transition and pure stone-like regimes can be manually turned on/off. Also note that the pure stone-like regime can be enforced in the algorithm by simply setting the transitional radius to zero.

Naturally, there is a coupling between the height of the sediment and settling dynamics. Here, we are assuming that the sediment varies with the cooling time scale Δt_c (i.e., we are decoupling sediment growth and crystal settling, this can be viewed as as extension of the quasi-steady state employed here).

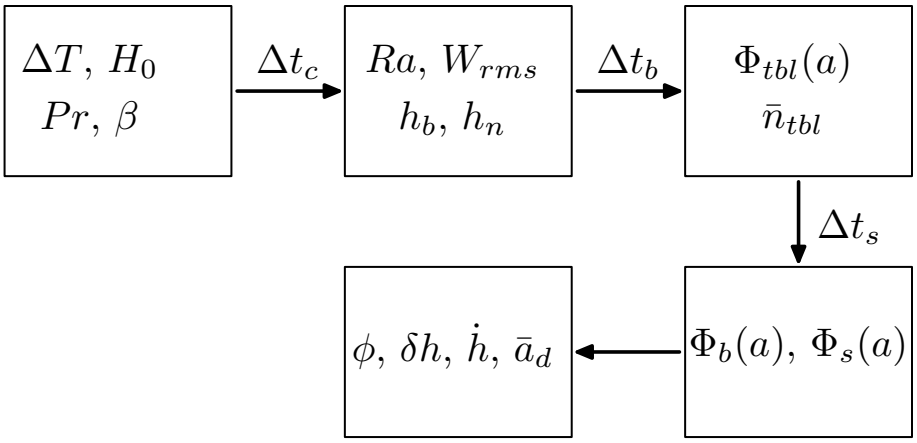

Figure 2.3: One time step Δt_c of the solidification loop - algorithm flowchart for the implementation of the quasi-steady state solver.

The flowchart of the proposed computational algorithm presented here is shown in Fig. 2.3. In the presented algorithm, the input variables are Prandlt number, temperature contrast ΔT, bulk undercooling β (i.e., $\beta = T_L - T_B$ and $\beta \geq 0$ K), and the initial height of the chamber H_0.

Moreover, we shall note that we developed the model in 1D and only the one-dimensional volume Δz came into play in spite of the nucleation amplitude having the spatial unit of inverse cubic meter. This implies the sediment height increment δh after one sedimentation iteration (for simplicity, we assume the sediment pile is perfectly packed) and the estimated rate of sedimentation shall be calculated as

$$\delta h = \frac{\Delta t_c}{\Delta t_s} \bar{n}_{\mathrm{s}} \frac{4}{3} \pi \sum_{i=1}^{n_b} n_i a_i^3 \; = \frac{\Delta t_c}{\Delta t_b} \bar{n}_{\mathrm{tbl}} \frac{4}{3} \pi \sum_{i=1}^{n_b} n_i a_i^3 \,, \tag{2.2}$$

$$\dot{h} = \frac{\delta h}{\Delta t_c} \,, \tag{2.3}$$

where $\bar{n}_{\mathrm{s}}$ and $\bar{n}_{\mathrm{tbl}}$ are steady-state numbers of crystals leaving the suspension and boundary layer per time steps Δt_s and Δt_b, respectively, and (n_i, a_i) denotes one bin of the normalized crystal size distribution in the sediment.

3. Results

This chapter is divided into three sections. In the first section, we investigate the boundary layer processes. Subsequently, we demonstrate several numerical tests and benchmarks. In the third section, we study different end-members and perform a reference run, followed by an exploration of the space of physical parameters (chamber height, temperature contrast, Prandtl number, undercooling, growth and kinetic laws amplitudes). Last but not least, we embark on a brief discussion in regard of the obtained results. Physical parameters and their ranges are listed in Table 3.1 below.

Table 3.1: Physical parameters

Parameter	Notation	Value	Unit
Initial height of the chamber[1]	H_0	10^1–10^4	m
Temperature contrast	ΔT	10^2–10^{-6}	K
Density of liquid phase[2]	ρ_F	2700	$\mathrm{kg\,m^{-3}}$
Density of solid phase[2]	ρ_C	2800	$\mathrm{kg\,m^{-3}}$
Thermal diffusivity [3]	κ	5×10^{-7}	$\mathrm{m^2\,s^{-1}}$
Thermal expansivity[4]	α	5×10^{-5}	$\mathrm{K^{-1}}$
Gravitational acceleration	g_0	9.8	$\mathrm{m\,s^{-2}}$
Latent heat of crystallization[2]	$\mathcal{L}$	4×10^5	$\mathrm{J\,kg^{-1}}$
Thermal capacity[2]	c_p	1.3×10^3	$\mathrm{J\,kg^{-1}\,K^{-1}}$
Prandtl number [5]	Pr	10^3–10^5	–
Critical Rayleigh number [6]	Ra_{cr}	660	–
Kinematic viscosity	ν	$Pr \cdot \kappa$	$\mathrm{m^2\,s^{-1}}$
Liquidus temperature[7]	T_L	1400	K
Solidus temperature[7]	T_S	1200	K
Nucleation delay	ε	10–60	K
Bulk undercooling	β	0–250	K
Nucleation amplitude[7]	N_0	10^1–10^5	$\mathrm{m^{-3}\,s^{-1}}$
Growth amplitude[7]	G_0	10^{-4}–10^{-10}	$\mathrm{m\,s^{-1}}$
Nucleation maximum[7]	T_I^*	0.81–0.92	–
Growth maximum[7]	T_G^*	0.93–0.95	–
Scaling factor (Nusselt number)[8]	c_{Nu}	0.16	–
Scaling factor (Reynolds number)[8]	c_{Re}	0.43	–

Adapted from:

[1] Frank Press [2000].
[2] Jarvis and Woods [1994].
[3] Ni et al. [2015].
[4] Solomatov [2004].
[5] Martin and Nokes [1989].
[6] Turcotte and Schubert [2014].
[7] Hort [1997].
[8] Ahlers et al. [2009], Kraichnan [1962].

3.1 Boundary layer

First, we are going to investigate the behavior of crystals in the TBL. Due to temperature contrast ΔT, the growth rate varies across the whole layer. In Fig. 3.1, the residence time of each crystal family is plotted against its nucleation depth (i.e., the depth at which the family was nucleated, measured from the chamber roof) for two values of the temperature contrast ΔT. Depending on the magnitude of the nucleation delay ε, $h_\mathrm{b}/h_\mathrm{n}$ ratio, temperature contrast ΔT, and their mutual relationship (i.e., $\Delta T \geq \varepsilon$ or $\Delta T < \varepsilon$), the TBL residence time against nucleation depth can exhibit substantially different behavior. For certain setups, we observe counter-intuitive behavior: Crystals closer to the bottom of the nucleation sublayer need more time to gravitationally fall out of the thermal boundary layer when compared to crystals nucleated closer to the roof (see the black line in Fig. 3.1). This is because undercooling decreases with increasing distance from the roof, resulting in smaller hence slower crystals there. Surprisingly, the final crystal size distribution $\Phi_\mathrm{tbl}(a)$ does not seem to reflect it.

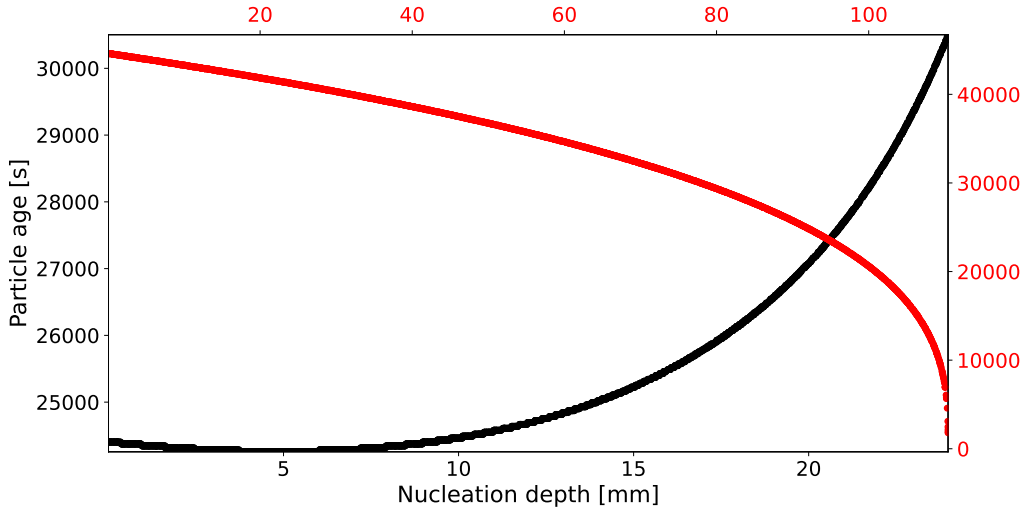

Figure 3.1: Residence time in the thermal boundary layer against nucleation depth: demonstration of the paradox for Hortian laws (for $T_I^* = 0.92$ and $T_G^* = 0.95$, corresponding lag $\varepsilon \approx 23$ K, $G_0 = 1 \times 10^{-8}$ m s^{-1}, $N_0 = 1 \times 10^3$ m^{-3} s^{-1}) for $\Delta T = 60$ K (black line) and $\Delta T = 1$ K (red line), and $\beta = 0$ K. Results obtained for one generation (i.e., the 0-generation method), $H_0 = 10^3$ m and $Pr = 1 \times 10^3$.

In Fig. 3.2, we demonstrate how the steady state is reached for the TBL processes by studying the crystal flux into the bulk with the step-by-step method. Subsequently, Fig. 3.3 displays the steady state distribution $\Phi_\mathrm{tbl}(a)$. Even when ΔT is very small and the growth rate is effectively contrast across the layer, the TBL distribution spans over a relatively large interval of radii and the shape does not change due to the scaling of the boundary thickness as $\Delta T^{-1/3}$.

Now, a brief aside: the TBL concept in the thesis is idealized - we are assuming a spatially uniform boundary layer of constant thickness, but this is not what is actually occurring. In reality, the boundary layer is expected to be spatially heterogeneous, experiencing local episodes of diffusive growth following $h_b(t) \sim (\kappa t)^{1/2}$. Upon reaching the critical thickness $h_{b,\mathrm{cr}}$, a segment of the boundary

layer breaks off thereby becoming a cold downwelling plume. The characteristic plume release time scale (e.g., Turcotte and Schubert [2014]) follows

$$t_p \sim \frac{1}{\kappa}\left(\frac{\nu\kappa Ra_{h,\mathrm{crit}}}{\alpha g \Delta T}\right)^{2/3}, \tag{3.1}$$

where $Ra_{h,\mathrm{crit}}$ is the critical Rayleigh number (Table 1).

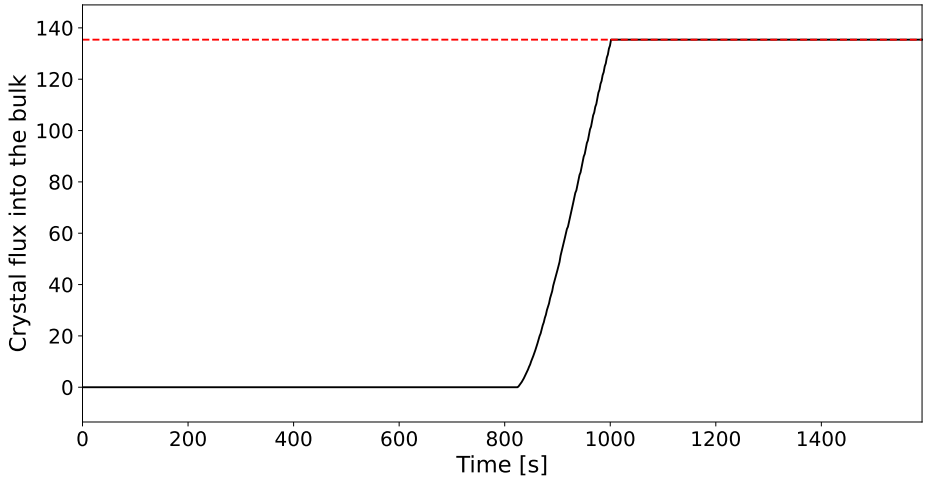

Figure 3.2: Crystal flux entering the bulk (black) as a function of time. After a transient period, that is needed by the first crystals to fall through the entire TBL, the flux converges to the average number of crystals nucleated in the TBL per time unit (red). Same setup as in Fig. 3.1 and $\Delta T = 10^2$ K.

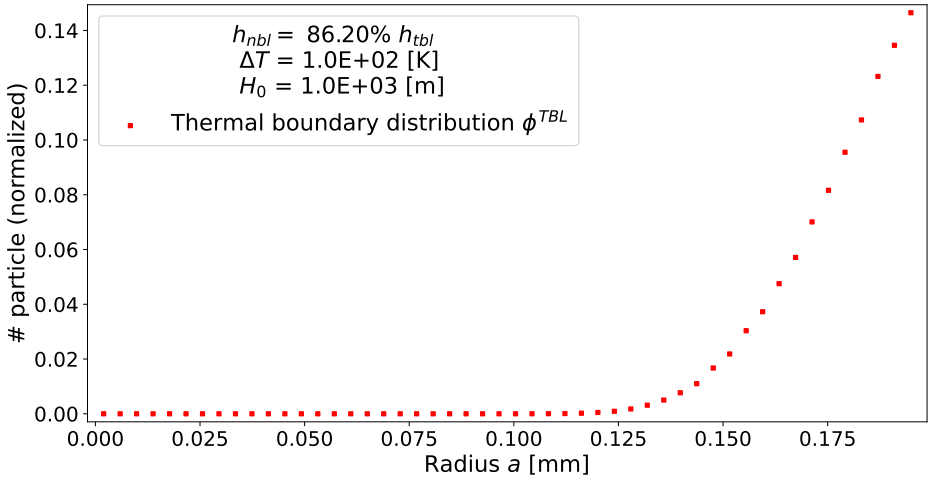

Figure 3.3: Steady-state TBL crystal size distribution falling into the convecting bulk for the growth and nucleation laws after Hort (see Eq. (1.33) and Eq. (1.34)). The minimum size of crystals is non-zero, because, when $h_b > h_n$, all crystals cross a region where nucleation does not occur but crystal growth does. Same setup as in Fig. 3.3.

A weak point of our theoretical model is that the TBL is considered to be a stable layer with a perfectly flat boundary, while in reality it undergoes local periodic collapses related to downwelling formations. This seems troubling in particular when the time scale t_p from Eq. (3.1) is (significantly) shorter than t_b in Eq. (1.15). For setups predicting $t_b > t_p$, we measured the residence time of each crystal and we mimic the plume advection by extracting the crystal as soon as the residence time reaches the time of the cold plume release. This approach strictly applies the transient boundary layer theory described in Turcotte and Schubert [2014], Chapter 8.6. We observe two consequences: a) radii of TBL crystals are (significantly) decreased, which brings us closer to the zero TBL crystal radius limit, and b) the TBL distribution is distorted or even collapsed into a quasi-Dirac distribution. In Section 3.3.1, we discuss the impact of the inflow distribution TBL on the results. Overall, such a modification has only little effect on the crystal size distribution in the sediment, which is our primary target. On this account, we deem it acceptable to work within the gravitational settling framework.

3.2 Numerical tests

3.2.1 Distribution benchmark (special case)

To test the implementation of bulk processes, we first study the limiting case of dust-like particles with zero growth inside the convecting bulk (i.e., $T_B = T_L$, $\beta = 0$). In this case, the crystal growth occurs only in the TBL. For $\mathcal{G}(T_B) = 0$, the quasi-steady approach implies that the size distributions falling into the bulk and leaving the suspension shall match. Moreover, dust-like crystals settle preferentially as $\sim a^2$. The numerical simulation is therefore expected to yield the following:

$$\Phi_{\mathrm{tbl}}(a) = \Phi_{\mathrm{sed}}(a)\,, \tag{3.2}$$

$$\Phi_{\mathrm{sed}}(a) = a^2 \Phi_{\mathrm{blk}}(a)\,. \tag{3.3}$$

We carried out two benchmark simulations (for sample values $H_0 = 10^2$ m and $\Delta T = 10^2$ K) for linear nucleation and growth laws (Fig. 3.4) and laws after Hort (Fig. 3.5). In both cases, the expected result is obtained. Note that the two benchmarks were conducted for greatly different growth amplitudes and different nucleation lags, and also ΔT was large such that the Hortian curves cannot be approximated by linear laws over the TBL temperature range, hence the overall different distributions.

3.2.2 Crystal tracing vs. Method of distributions

In Chapter 2, we introduced two ways of handling the sedimentation process inside the bulk, the method of distributions (*mDis*) and the method of crystal tracing (*mTac*). The latter allows us to implement stone-like particles into the system and is therefore applicable to a broad range of natural settings. The method of distributions employs discretized histograms and is not capable of storing information about the volume in which the a crystal family remains effectively mixed (cf. Eq. (1.18)). For the method comparison, see Fig. 3.6 below.

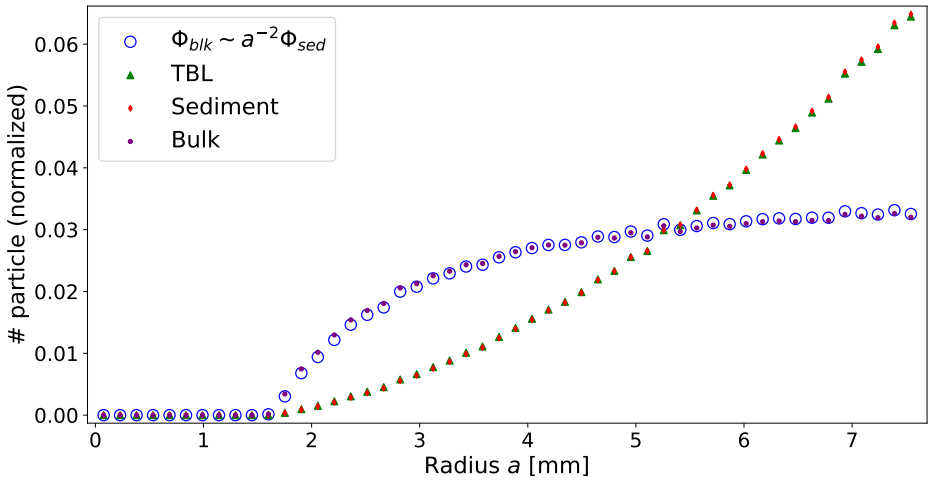

Figure 3.4: Zero bulk crystal growth run for linear laws, $N_{\text{pow}} = 5 \times 10^6$ m^{-3} s^{-1} and $G_{\text{pow}} = 1 \times 10^{-3}$ m s^{-1} and nucleation lag $\varepsilon = 10$ K.

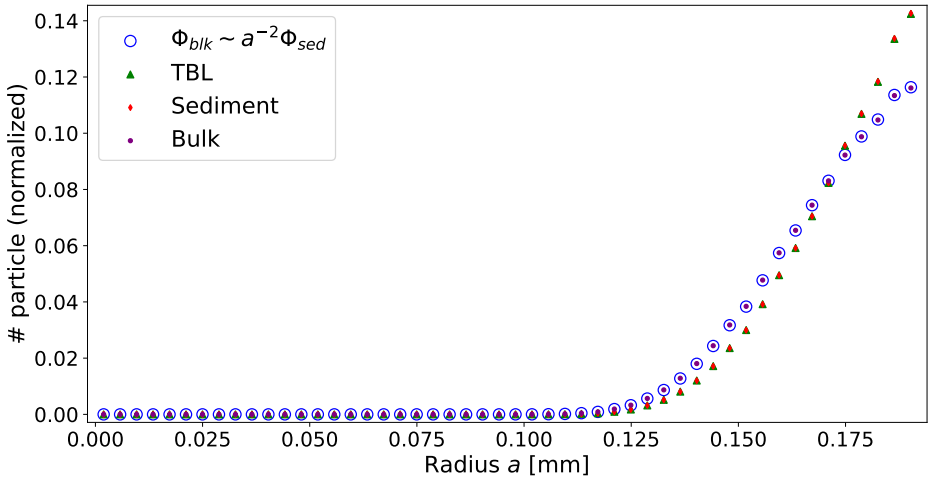

Figure 3.5: Zero bulk crystal growth run for laws after Hort (for $T_I^* = 0.92$ and $T_G^* = 0.95$, corresponding lag $\varepsilon \approx 23$ K), $N_0 = 1 \times 10^3$ m^{-3} s^{-1} and growth amplitude $G_0 = 1 \times 10^{-8}$ m s^{-1}.

There is a small discrepancy between both distributions, which can be minimized by the time step size, the number of time steps, and crystal cut-off (see Section 2.2). There is a numerical artefact at the tail of the distribution stemming from the nature of implementation for the histogram bin size adjustment. In contrast, the tracing method exhibits a longer tail that smoothly attenuates to zero. The mean radii predicted by these methods are typically within a 1% relative error.

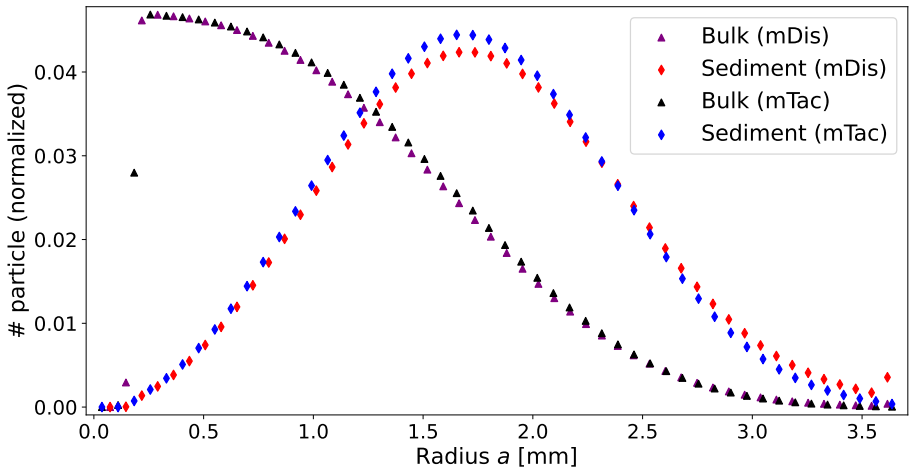

Figure 3.6: Computed bulk and sediment crystal size distributions $\Phi_{\text{blk}}(a)$ and $\Phi_{\text{sed}}(a)$: comparison of the method of distributions (purple and red) and crystals tracing (black and blue) for the pure dust-like settling regime for the sample values $H_0 = 10^3$ m, $\Delta T = 10^2$ K, and $\beta = 5$ K for nucleation and growth laws after Hort.

3.3 Parametric study

3.3.1 Dust-like regime: Analytical formula?

In the spirit of Section 1.2.1, we fitted the scaling functions to the computed crystal size distributions in the bulk and sediment (see Figs. 3.7–3.8), thus

$$\Phi_{\text{blk}} = A_1 \exp\left(-A_2 a^3\right) , \tag{3.4}$$

$$\Phi_{\text{sed}} = A_1 a^2 \exp\left(-A_2 a^3\right) . \tag{3.5}$$

Both coefficients A_2, thus the exponential weight factors, are in a very good accord with the form predicted in Eq. (1.28). In addition, $A_2^{-1/3}$ matches the calculated $\bar{a}_d$ perfectly for the bulk distribution and with a 12% deviation for the sediment distribution. Here, we do not make an attempt to map A_1 to a particular combination of parameters. Given the nature of the problem, however, A_1 is most likely influenced by the growth rate and nucleation rate in the TBL. Beware, we are not doing this with the expectation of a perfect agreement agreement - continuous influx of TBL crystals with non-zero radius clearly distorts the result (the following section addresses the question of how much); we merely wish to ascertain how closely we align with this theoretical result derived for the the single zero-sized population in Chapter 1.

3.3.2 Dust-like regime: Impact of TBL distribution?

On the previous page, we demonstrated that the characteristic shape of the steady state distribution in the sediment for purely dust-like settling regime is a quasi-Gaussian (for $\mathcal{G}(T_B) > 0$). In Fig. 3.9, the effect of the inflow distribution $\Phi_{\text{tbl}}(a)$ on $\Phi_{\text{sed}}(a)$ is studied.

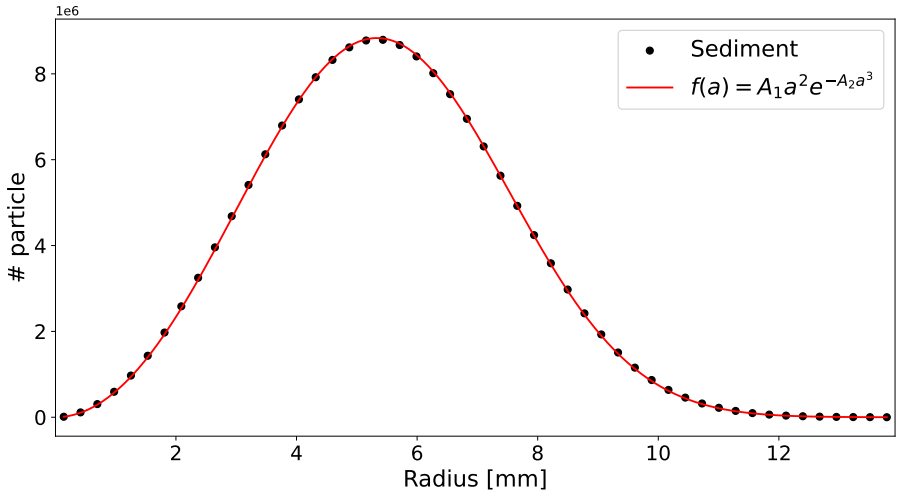

Figure 3.7: Fit of $f(a) = A_1 a^2 \exp(-A_2 a^3)$, A_2 matches $\lambda/3\mathcal{G}(T_B)(H_0 - h)$ with a deviation of 2.65 %. Simulation parameters: $H_0 = 10^3$ m, $Pr = 1 \times 10^3$, $G_0 = 1 \times 10^{-8}$ m s^{-1}, and $\Delta T = 100$ K.

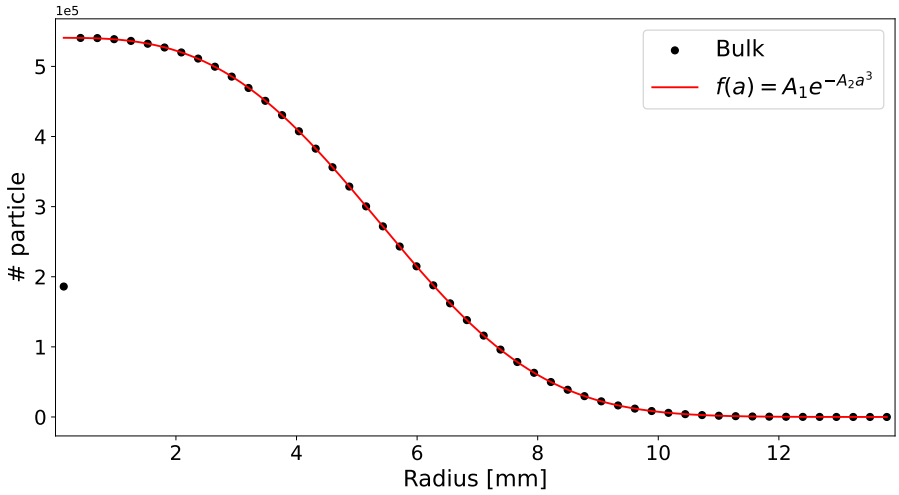

Figure 3.8: Fit of $f(a) = A_1 \exp(-A_2 a^3)$, the calculate coefficient A_2 matches $\lambda/3\mathcal{G}(T_B)(H_0 - h)$ with a deviation of 0.30 %. Parameters same as in Fig. 3.7.

As we mentioned at the beginning of this chapter, the TBL thickness scales as $\Delta T^{-1/3}$. When we reduce the temperature contrast (and consequently the Rayleigh number), the radius of TBL crystal increases as they need to travel a longer distance. As a result, the signature of the TBL distribution becomes more pronounced for small temperature contrasts.

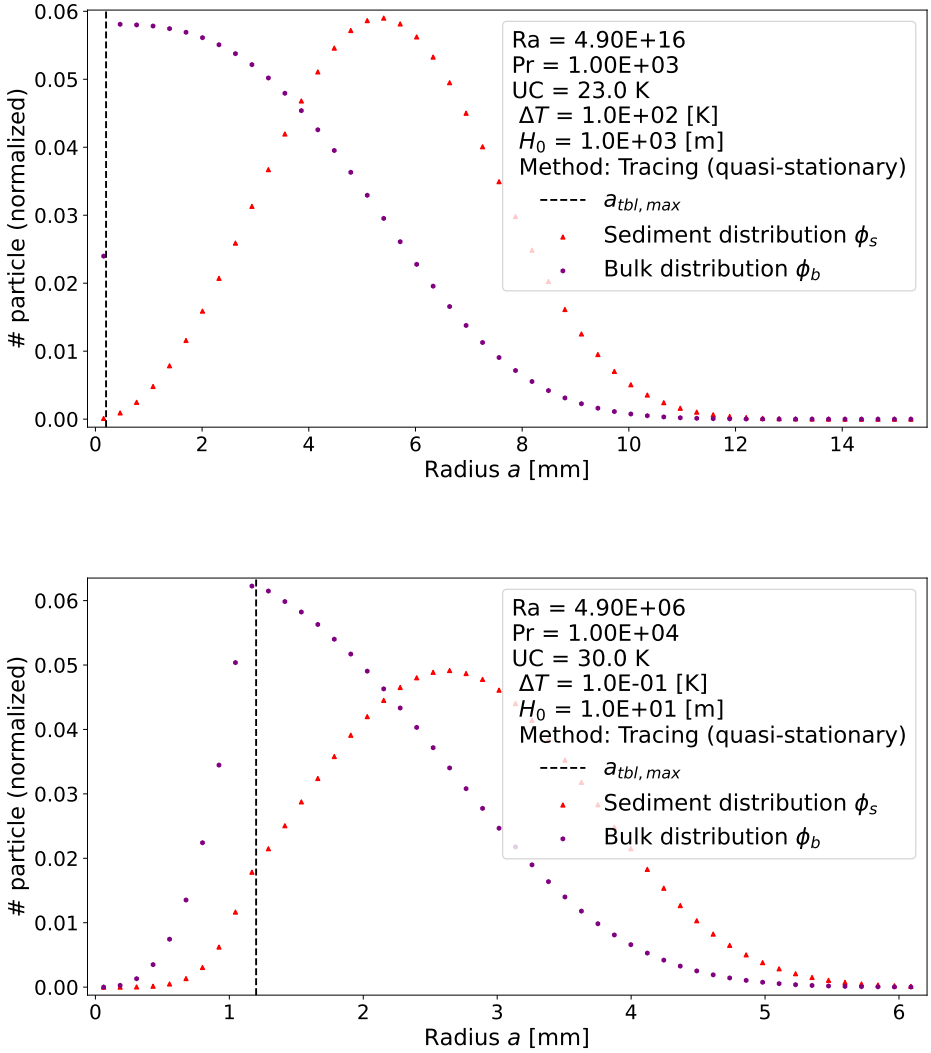

Figure 3.9: Demonstration of the impact of TBL distribution when $a_0 \ll \mathcal{G}(T_B)t_{\text{res}}$ is not satisfied. Dashed line labels the maximum crystal radius falling into the bulk. Stone/dust transition is manually turned off.

3.3.3 Dust-like regime: What factors influence the mean radius?

The fits conducted earlier insinuated that mean radius is directly linked to the system parameters. In this section, we investigate how the mean crystal radius in the sediment scales with various model parameters. Figs. 3.10–3.13 demonstrate that the sediment distribution does not respond to the temperature contrast ΔT, unless the maximum crystal radius attained in the thermal boundary layer becomes comparable to the mean crystal radius in the bulk (satisfied for small chambers and low temperature contrasts, hence low Rayleigh numbers). We observe that the mean crystal radius of Φ_{sed} scales as

$$\bar{a}_d \sim [(H_0 - h)Pr\mathcal{G}]^{1/3} \sim [(H_0 - h)\nu\mathcal{G}]^{1/3} \ , \tag{3.6}$$

which is, again, consistent with Eq. (1.28), i.e., with the exercise in which zero-sized crystals are uniformly distributed in the bulk. Considering the small devi-

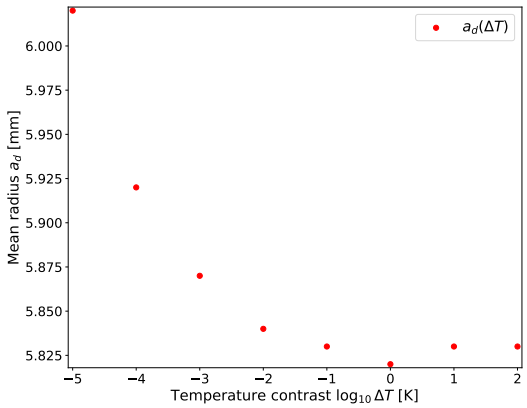

Figure 3.10: Mean radius of Φ_{sed} as a function of the temperature contrast ΔT. Other parameters fixed at the values $H_0 = 1 \times 10^2$ m, $Pr = 1 \times 10^4$, and $G_0 = 1 \times 10^{-6}$ m s^{-1}.

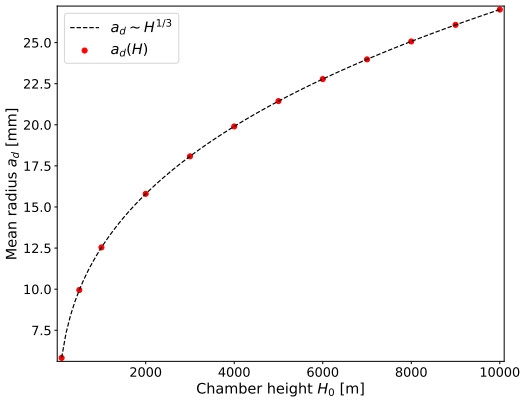

Figure 3.11: Mean radius of Φ_{sed} as a function of the height chamber H_0. Other parameters fixed at the values $\Delta T = 1$ K, $Pr = 1 \times 10^4$ and $G_0 = 1 \times 10^{-6}$ m s^{-1}.

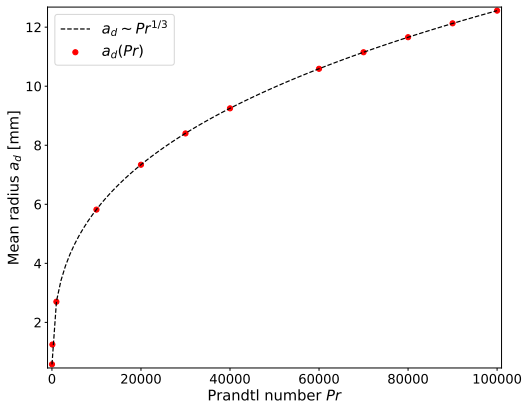

Figure 3.12: Mean radius of Φ_{sed} as a function of the Prandtl number Pr. Other parameters fixed at the values $\Delta T = 1$ K, $H_0 = 1 \times 10^2$ m and $G_0 = 1 \times 10^{-6}$ m s^{-1}.

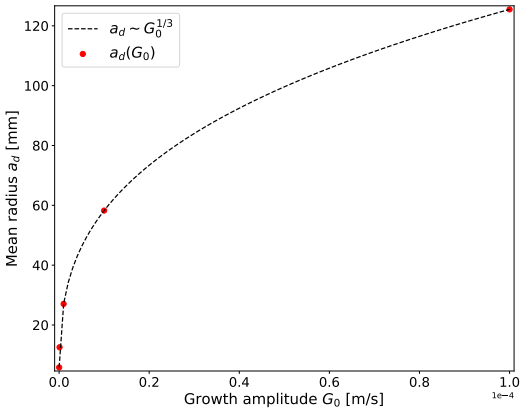

Figure 3.13: Mean radius of Φ_{sed} as a function of the growth amplitude G_0. Other parameters fixed at the values $\Delta T = 1$ K, $Pr = 1 \times 10^4$, and $H_0 = 1 \times 10^2$.

ation we observed in the fit, the constant of proportionality is expected to be of order $\sim \mathcal{O}(\lambda\nu)$. Again, lower temperature contrasts are associated with the TBL distribution being visible in the shape of Φ_{sed}, but the impact on the mean radius is marginal.

3.3.4 Impact of stone-like settling on the resulting distributions

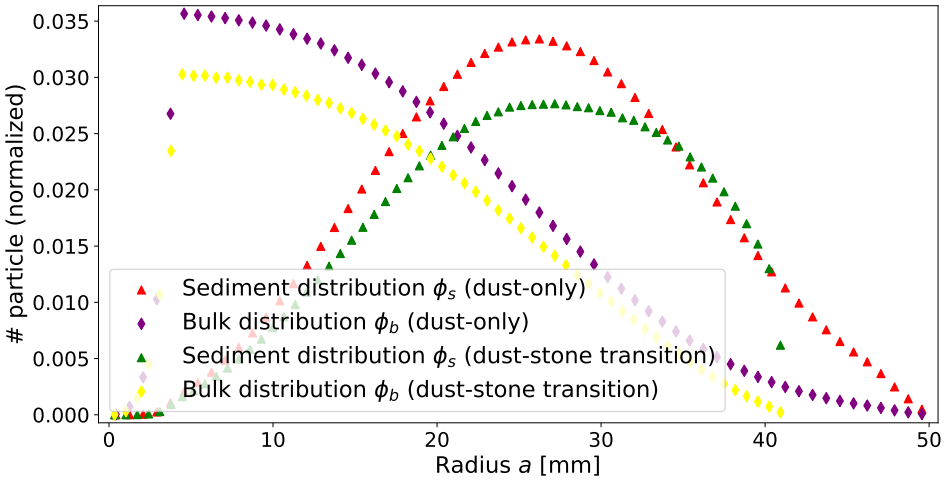

Figure 3.14: Run with the i) pure dust-like regime, stone/dust turned off (red - $\Phi_{\mathrm{sed}}(a)$, purple - $\Phi_{\mathrm{blk}}(a)$), and ii) stone/dust transition turned on (green - $\Phi_{\mathrm{sed}}(a)$, yellow - $\Phi_{\mathrm{blk}}(a)$) for the following parameters: $\Delta T = 1$ K, $H_0 = 10^2$ m, $\beta = 29$ K, $Pr = 1 \times 10^4$, and $G_0 = 1 \times 10^{-6}$ m s^{-1} (i.e., $\mathcal{G} = 7 \times 10^{-7}$ m s^{-1}). The transitional growth rate predicted by Eq. (3.8) gives $\mathcal{G}_{\mathrm{tr}} \approx 1 \times 10^{-7}$ m s^{-1}, so we can already see a minor skew.

When the Stokes velocity of a crystal becomes comparable to the mean flow velocity W_{rms}, the exponential decay law of Martin and Nokes is no longer applicable. With the onset of stone/dust transitional behavior, crystal settling becomes more effective. Consequently, we observe a downtick in the population of large crystals, manifested by a skew and a cut-off of the characteristic quasi-Gaussian (Fig. 3.14). It is useful to have an apriori insight as to whether or not stone-like settling is expected for a given set of model parameters. To this end, we conduct the following analysis: Crystals settle in the dust-like regime when $W_{\mathrm{rms}} \gtrsim W_S(a)$, as we argued earlier, the exponential decay law is a good approximation even for, e.g., $W_S/W_{\mathrm{rms}} \sim 0.5$. Invoking Eq. (1.3) and Eq. (1.5) yields

$$\kappa^{1/9}\alpha^{2/9}\Delta T^{2/9}(H_0 - h)^{1/6}\nu^{4/9}\rho_F^{1/2}\Delta\rho^{-1/2}g^{-5/18} \gtrsim a\,. \tag{3.7}$$

Relaxing this constraint for crystals with the mean radius given by Eq. (3.6) gives the following condition for the growth rate that must be satisfied for the stone-like regime to be neglected:

$$\kappa^{1/3}\Delta\rho^{-1/2}(H_0 - h)^{-1/2}\rho_F^{1/2}g^{1/6}\nu^{1/3}\alpha^{2/3}\Delta T)^{2/3} \gtrsim \mathcal{G}\,. \tag{3.8}$$

3.3.5 The influence of ΔT and G_0

As explained in Introduction, the main focus of this work is to predict how the magma dynamics are imprinted in the microstructure of the sediment. We discussed the role of ΔT as the quantity driving convection, and that its value is poorly constrained. Motivation for varying the growth amplitude is explained in Section 3.3.7. Figs. 3.15–3.16, we perform a series of simulations for a broad range of ΔT and for two values of G_0, with the remaining parameters being set to values centred in the middle of expected ranges: $H_0 = 10^3$ m, $\beta = 29$ K, and $Pr = 1 \times 10^4$). We choose ΔT from the interval $\in [10^2 - 10^{-6}]$ K and the two growth amplitude are $G_0 = 1 \times 10^{-6}$ m s^{-1} and $G_0 = 1 \times 10^{-8}$ m s^{-1} (N_0, T_G^*, and T_I^* same as in Fig. 3.5). We compute the steady-state (normalized) bulk and sediment crystal size distribution. Each run is characterized by the mean radius $\bar{a}_d$, temperature contrast ΔT and the corresponding transition radius a_{tr}. As crystals fall into the bulk, their radii are first small compared to the transition radius and they are thus effectively mixed within the entire liquid volume. As soon as they reach the transition radius, the volume they occupy begins to shrink. The portion of time that crystals spent in the dust-like regime (averaged over all crystals), is labeled as dust-duration in Figs. 3.15–3.16.

3.3.6 End-member scenarios

A quick inspection of the case study above gives us an insight into the shape of the resulting distributions. We can identify four distinct end-members:

i) Pure dust-like.

ii) Dust-like dominance.

iii) Stone-like dominance.

iv) Pure stone-like.

Ad i), see panel 1 in Fig. 3.15 and panels 1–3 in Fig. 3.16, this end-member is characterized by the already well-established quasi-Gaussian distribution. For large enough chambers, the influence of the inflow TBL distribution is negligible and the distribution is symmetric. The mean radius then does not depend on the temperature contrast.

Ad ii), see panel 2–3 in Fig. 3.15 and panel 4–6 in Fig. 3.16, crystals following this end-member gradually transition from dust-like to stone-like regime. As the amount of time spent as dust particles decreases, the deformation of the quasi-Gaussian becomes more substantial, the distribution peak eventually diminishes. The mean radius exhibits a weak declining trend with the temperature contrast.

Ad iii), see panels 4–5 in Fig. 3.15 and panel 7 in Fig. 3.16, crystals in this regime settle predominantly as stone-like particles. They do, however, behave as dust-like particles for a brief moment, thereby become well mixed upon entering the bulk. The volume they effectively occupy begins to shrink shortly after, as their radius quickly reaches the transition radius. This end-member is characterized by a distribution akin to the one we observe in the thermal boundary layer.

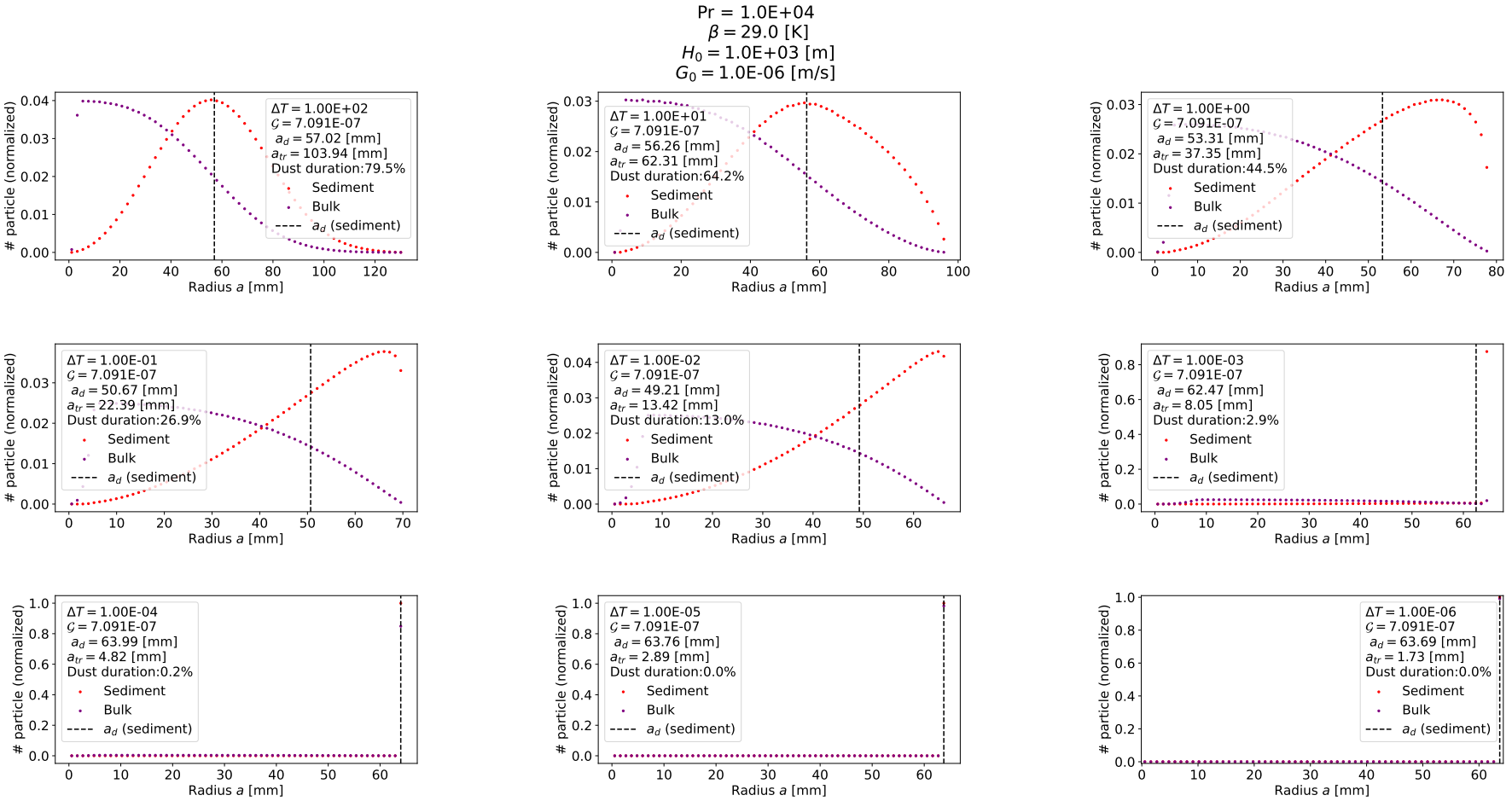

Figure 3.15: Reference run for $G_0 = 1 \times 10^{-6}$ m s^{-1} investigating dependence of the mean radius and final distributions shape on the temperature contrast ΔT.

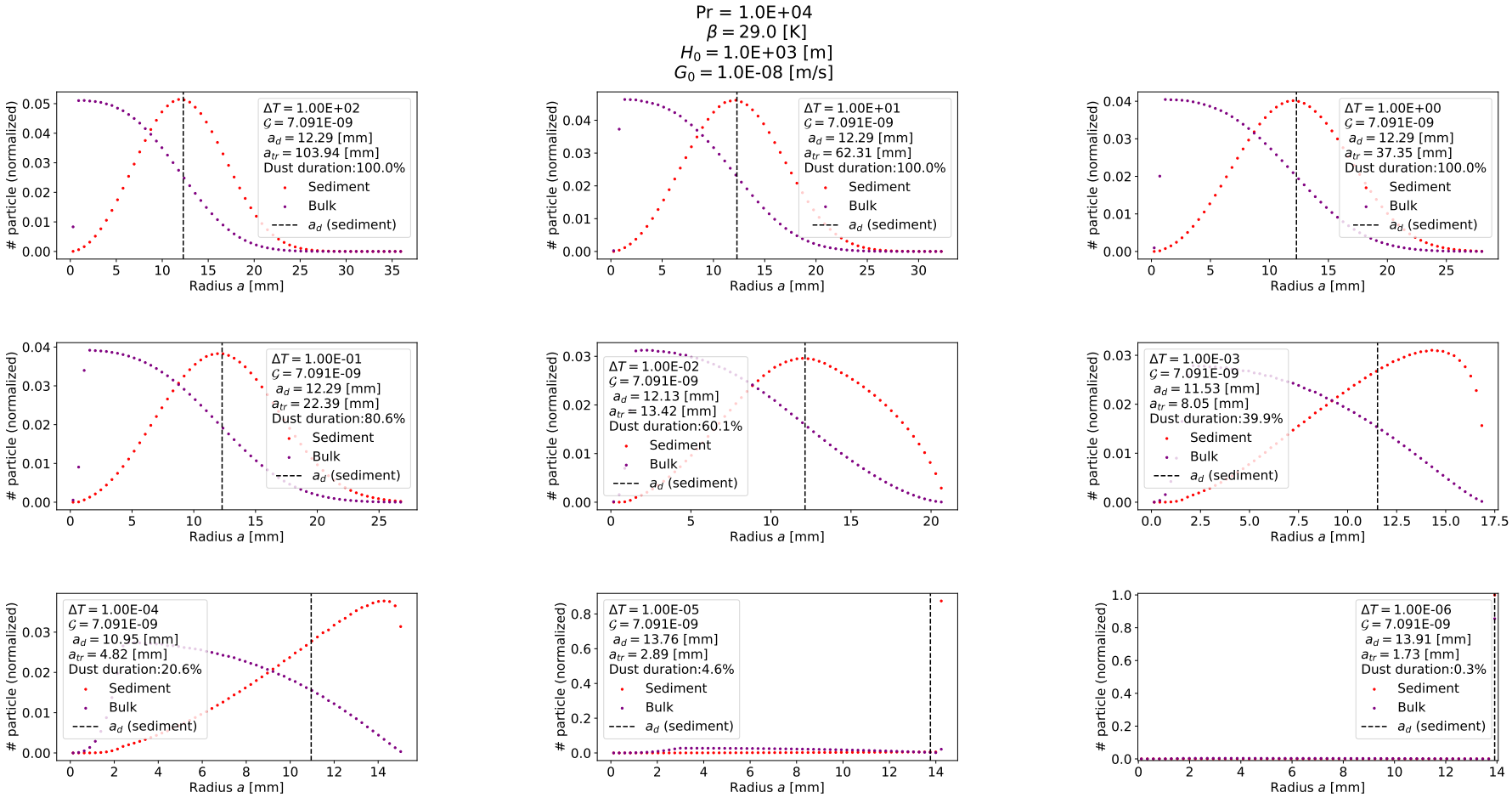

Figure 3.16: Reference run for $G_0 = 1 \times 10^{-8}$ m s^{-1}, investigating dependence of the mean radius and final distributions shape on the temperature contrast ΔT.

Ad iv), see rest of the panels in Figs. 3.15–3.16, radii of crystals extracted from the boundary layer are already greater than the transitional radius. The crystal growth occurs primarily in the bulk and the radius difference amongst incoming crystals is small, which results in all crystals having nearly the same radius upon reaching the base of the chamber. It is characterized by a sudden noticeable uptick in the mean radius (in comparison to cases ii) and iii), where we observe a declining trend).

3.3.7 Model space exploration

The following section covers a thorough exploration of the model space, with a focus on the mean radius and the sedimentation rate. The considered ranges for the height of the chamber and temperature contrast are $H_0 \in [10^2 - 10^4]$ m, $\Delta T \in [10^2 - 10^{-6}]$ K. We performed simulations for two different values of the bulk temperature T_B (corresponding to undercooling $\beta = 29$ K and $\beta = 200$ K), two values of the growth amplitude ($G_0 = 1 \times 10^{-6}$ m s^{-1} and $G_0 = 1 \times 10^{-8}$ m s^{-1}), two values of Prandtl numbers ($Pr = 1 \times 10^3$ and $Pr = 1 \times 10^5$), and with the nucleation rate being fixed $N_0 = 1 \times 10^3$ m^{-3} s^{-1}. The results are presented in the form of contour plots (see Figs. 3.18–3.19) for the mean radius a_d and the sedimentation rate $\dot{h}$, and 3D surface plots (see Figs. 3.17) displaying how dust-duration varies in the model parameter space.

Inspection of Figs. 3.18–3.19 indicates that the sedimentation rates obtained for some models are very high. If we invoke the scaling expression for the mean crystal radius in the sediment,

$$\bar{a}_d \sim [(H_0 - h)\mathcal{G}Pr]^{\frac{1}{3}} \ , \tag{3.9}$$

and summon the scaling relation for the increase in sediment height, $\dot{h} \sim \bar{a}_d^3$, we can see that the sedimentation rate is very sensitive to any change in $\bar{a}_d$, and hence strongly responds to changes in the following parameters: the chamber height, growth rate amplitude, and Prandtl number. Height of the intrusion is an inherent characteristic, Prandtl numbers are well-measured, so we are left with the uncertainty in the growth amplitude. A number of older papers from the 1970s (e.g., Scherer and Uhlmann [1976]) dedicated to the study of crystal kinetics demonstrate that a change in the chemical composition of a laboratory prepared sample can lead to orders of magnitude difference in the growth rate. It should also be noted that the sedimentation rate depends linearly on the nucleation amplitude N_0, a shift in N_0 is therefore equally impactful. Large values of the sedimentation rates, stemming from large predicted mean crystal radii, lead to vanishingly small solidification times, often violating the assumption of the quasi-steady approach. While it is difficult to constrain the solidification time of an intrusion from geological and petrological measurements, seismic tomography indicates that the solidification time is rather short when compared to geological time scales (e.g., Sinton and Detrick [1992]). Note, however, that the solidification rates obtained within the quasi-steady framework employed here cannot be directly extrapolated to estimate the solidification time of the entire intrusion.

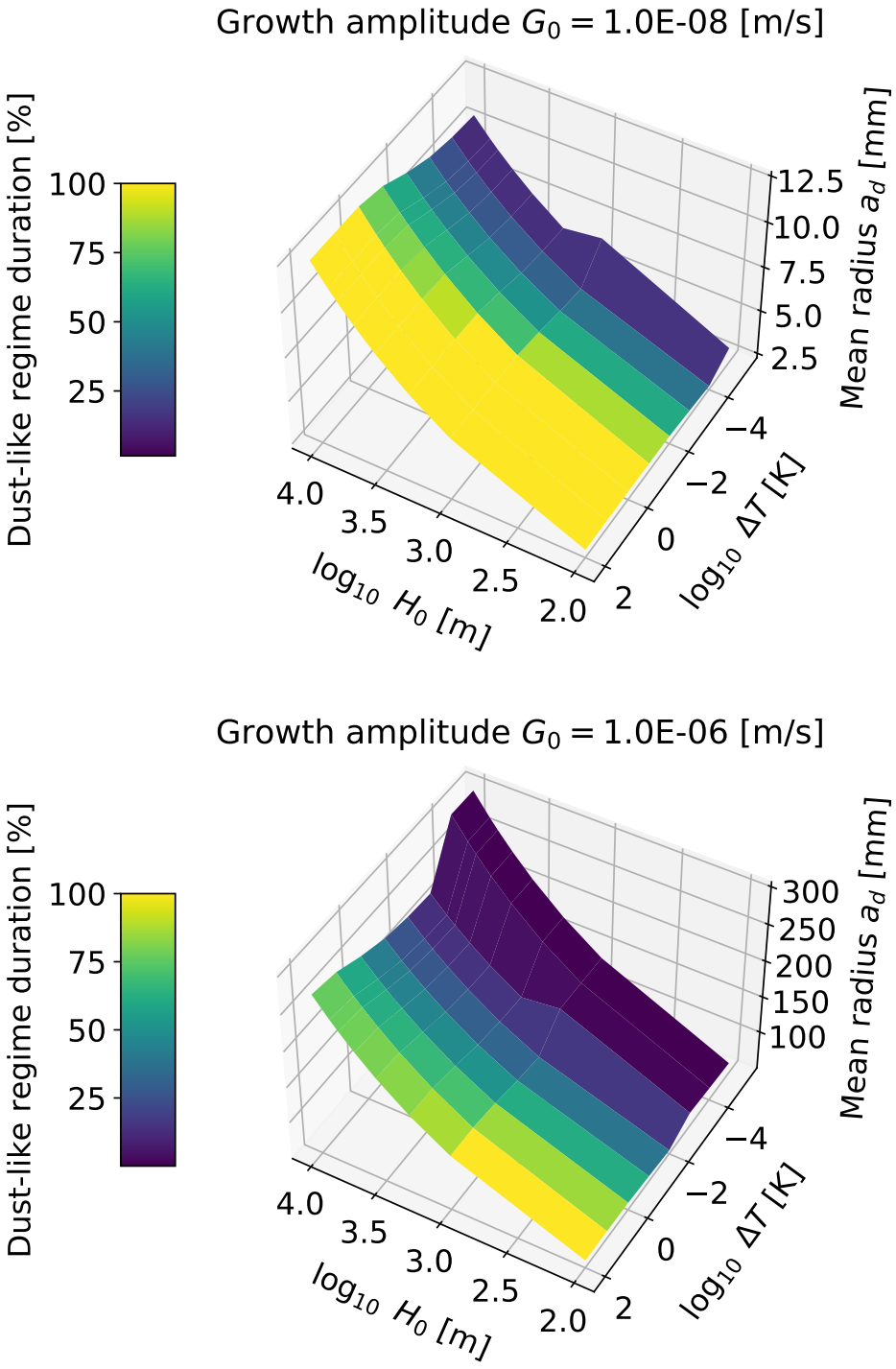

Figure 3.17: Mean radius in the sediment against temperature contrast ΔT (log scale) and chamber height H_0 (log scale), the surface is colored in accordance to the average dust-duration, for $Pr = 1 \times 10^4$ and $G_0 = 1 \times 10^{-8}$ m s^{-1}, (top image) and $Pr = 1 \times 10^5$ and $G_0 = 1 \times 10^{-6}$ m s^{-1} (bottom image).

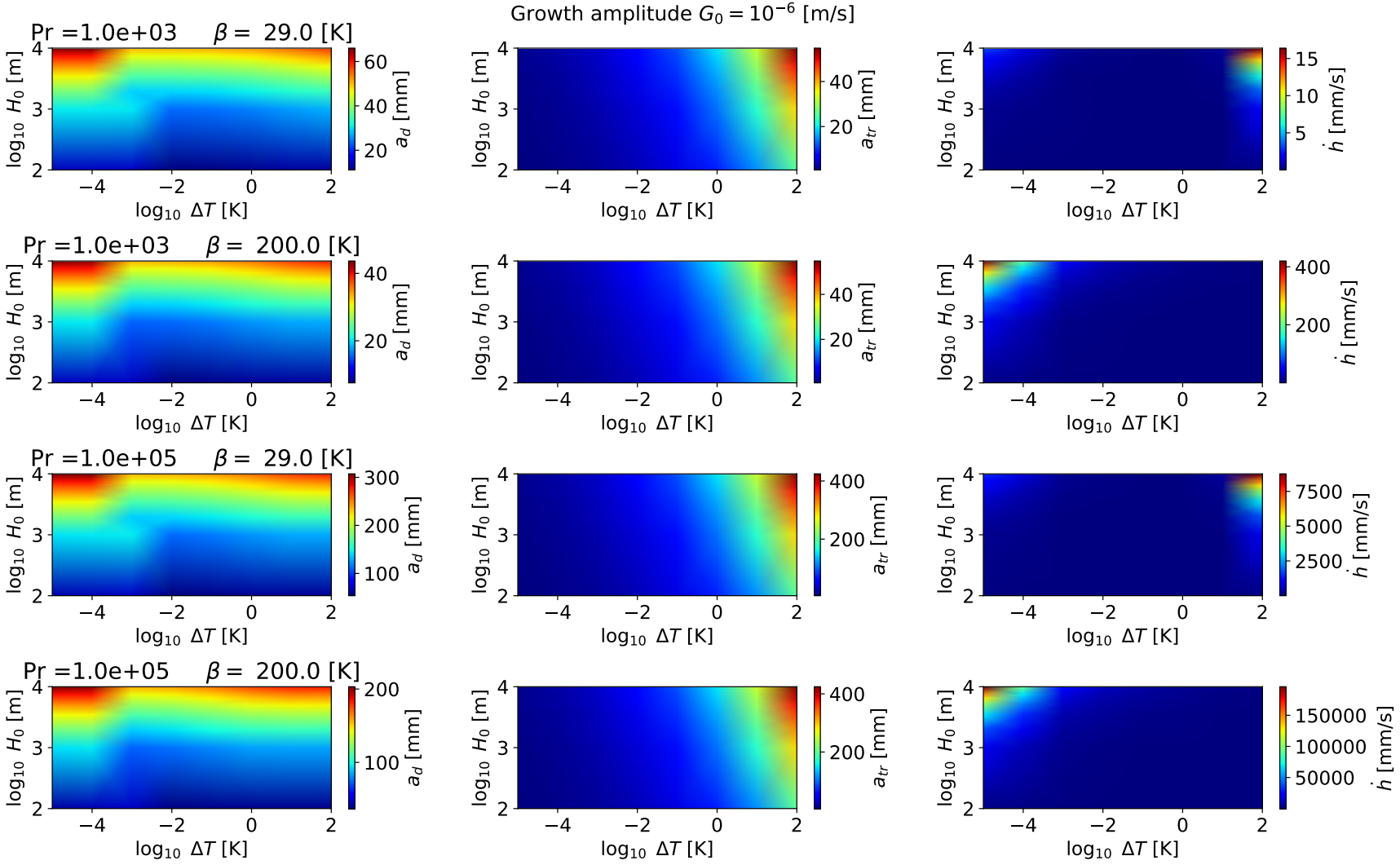

Figure 3.18: Parametric study (mean radius, transient radius, sedimentation rate) against chamber height, temperature contrast, Prandtl number (kinematic viscosity), and undercooling for growth amplitude $G_0 = 1 \times 10^{-6}$ m/s. Each contour figure comprises 8×8 models.

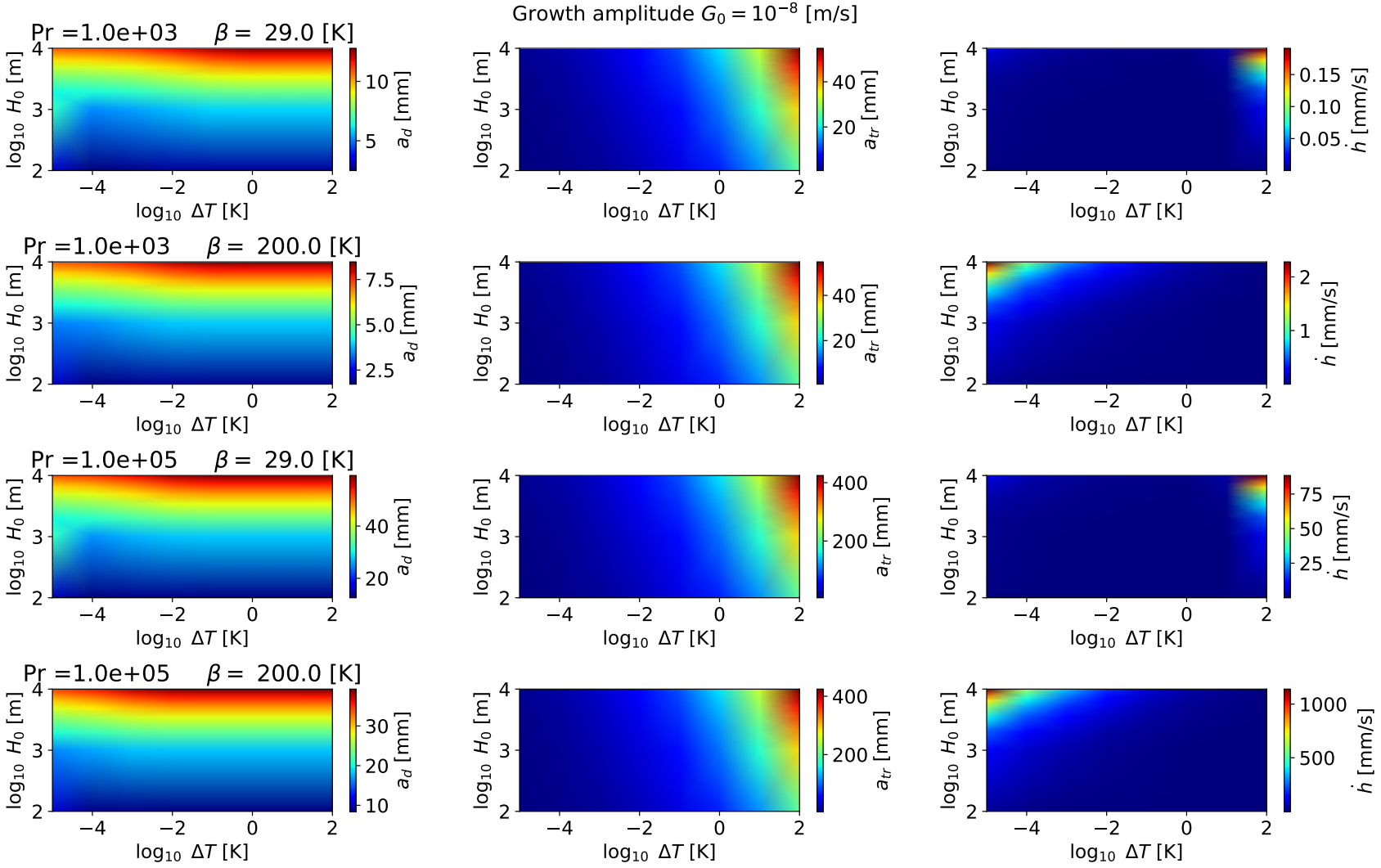

Figure 3.19: Parametric study (mean radius, transient radius, sedimentation rate) against chamber height, temperature contrast, Prandtl number (kinematic viscosity), and undercooling for growth amplitude $G_0 = 1 \times 10^{-8}$ m s^{-1}. Each contour figure comprises 8×8 models.

This is because, as the chamber begins to solidify, its chemical composition begins to evolve, and this is not accounted for in Chapter 3. If fractional crystallization takes place, the liquidus temperature of the residual magma evolves with time, and it is the time evolution of T_L and T_B that controls the solidification progress. In the next chapter, we outline how the model developed here could be used in future to capture the microstructure of a progressively solidifying chamber, whose temperature profile evolves self-consistently with time.

In contrast, the mean radii can be analyzed in the microstructure records - the characteristic crystal size observed in the sediment ranges around 1 mm, with 1 cm being the upper bound (e.g., Holness et al. [2017], Holness [2022]). The parametric study above provides us with a way to impose lower bounds for the growth amplitude or undercooling reached during the chamber history. To match the observed mean radii, the growth rate should be of order $\mathcal{G} \sim 1 \times 10^{-8}$ $\mathrm{m\,s^{-1}}$ or lower (cf. Figs. 3.18–3.19).

We also observe that the dust-like regime dominance is restricted to higher temperature contrasts. If ΔT driving the thermal convection is truly as small as Martin and Nokes [1988] argues, stone-like settling dynamics should dominate. The pure stone-like regime and the collapse of the distribution into a quasi-Dirac distribution is associated with extremely small temperature contrasts. However, this is not what is observed in real intrusions! Records of microstructure are always characterized by non-trivial distributions. This observation favors Turner and Huppert and insinuates convection in magma chambers is truly vigorous. Since each settling dynamics leave a characteristic footprint in the sediment microstructure, we believe the results presented here could help to guide future microstructure analysis to unravel the workings of the solidification process.

4. Outlook: Full solidification

4.1 Temporal evolution of temperature inside the chamber

The model presented above was built to capture the crystal size distribution of the sediment when the temperature profile inside the magma chamber is given. Both temperature-related variables, ΔT and T_B, governing the crystallization kinetics and thermal convection vigor were free and chosen ad hoc from a wide range. In a real system, heat is gradually extracted from the reservoir and both $\Delta T(t)$ and $T_B(t)$ are time-dependent. In this chapter, it is outlined how we plan to compute the thermal history of the body, in order to evaluate how the crystal size distribution in sediment evolves with height of the sediment, i.e. with the progress of solidification.

In the big-tank hypothesis, a large volume of magma is injected into a host rock, whose temperature profile can be estimated by solving the 1D heat equation,

$$\frac{\partial T_{bg}(z,t)}{\partial t} = \kappa_{\mathrm{bg}}(z)\frac{\partial^2 T_{bg}(z,t)}{\partial z^2}\,, \quad z \in \mathcal{D},\ t \in (0, t_0)\,. \tag{4.1}$$

where $\mathcal{D}$ denotes the studied domain (crust or lithosphere) and $\kappa = k/\rho c_p$ is the depth-dependent thermal diffusivity of the host rock. The initial condition $T_{\mathrm{bg}}(0) = T^0_{\mathrm{bg}}$ and imposed boundary conditions (Dirichlet/Neumann) correspond to the geological setting. The background profile is computed at an arbitrary time of magma emplacement t_0.

Once the liquid magma of temperature $T_m > T_{\mathrm{bg}}$ fills a formed cavity, the temperature profile drastically changes (Fig. 4.1).

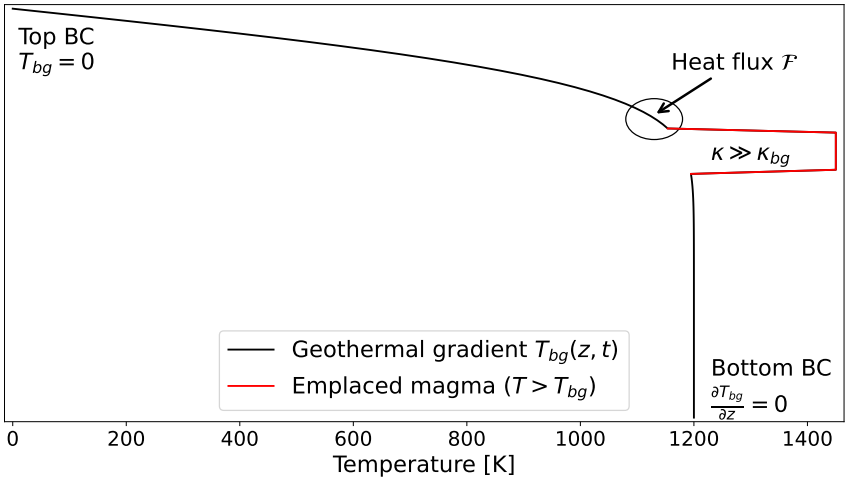

Figure 4.1: Sketch of the geothermal profile after the magma emplacement (red skew). By measuring the temperature gradient at the top of the chamber, we can directly calculate the extracted heat flux and link it to the temperature contrast driving the thermal convection inside the chamber.

When thermal convection in the low-viscosity magma is initiated, the heat transfer across the chamber is no longer via conduction. To mimic convection within the framework of Eq. (4.1), one can introduce an "effective" thermal diffusivity κ_{eff} in the liquid region, for which it holds that $\kappa_{\text{eff}} \gg \kappa_{\text{magma}}$, where κ_{magma} is the actual material parameter describing heat diffusivity of the emplaced liquid. To account for the release of latent as the liquid gradually solidifies, Eq. (4.1) needs to be modified also by adding a heat source. Altogether, the 1D temperature evolution after magma emplacement can be estimated by solving the following equation,

$$\frac{\partial T(z,t)}{\partial t} = \kappa_{\text{mod}}(z,t)\frac{\partial^2 T}{\partial z^2} + \frac{1}{c_p}L(z,t)\,, \tag{4.2}$$

$$\kappa_{\text{mod}}(z,t) = \begin{cases} \kappa_{\text{eff}} & \text{liquid region}\,, \\ \kappa_{\text{sed}} & \text{formed sediment}\,, \\ \kappa_{\text{bg}}(z,t) & \text{elsewhere}\,, \end{cases} \tag{4.3}$$

where $T(z,t)$ denotes the temperature profile after the formation of the chamber, c_p thermal capacity, $L(z,t)$ is the released latent heat of crystallization per time unit, and κ_{sed} is thermal diffusivity of the cumulate. As the sediment pile grows, the region, where $\kappa_{\text{mod}} = \kappa_{\text{eff}}$ holds, shrinks in volume.

In order to couple our microstructural model (Chapters 1–3) with the thermal history model, we need to compute T_B, ΔT, and T_L at any time t. The bulk temperature $T_B(t)$ can be obtained by averaging $T(z,t)$ over the liquid region. When thermal convection is mimicked by thermal diffusion with enhanced diffusivity, the temperature profile in the liquid region will not resemble the one depicted in Fig. 1.1 (TBL will not form). To determine the temperature contrast in the TBL, ΔT, one can assume that the convective vigor in the liquid is controlled by the amount of heat extracted by the host rock Carrigan [1988]. By measuring the temperature gradient, and thus the heat flux, in the vicinity of the roof of the chamber, we obtain the heat flux based Rayleigh number (e.g., Carrigan [1988]) for the convecting liquid magma as

$$Ra_{\mathcal{F}} = \frac{\alpha g \mathcal{F}(H_0 - h)^4}{k\kappa\nu}\,. \tag{4.4}$$

By comparing Eq. (4.4) with Eq. (1.1), we obtain a formula linking the numerically measured heat flux to the temperature contrast ΔT as

$$\Delta T = \frac{\mathcal{F}(H_0 - h)}{k}\,. \tag{4.5}$$

Magma is a multicomponent liquid and hence its solidus and liquidus temperature differs. We label the liquidus temperature of the initial bulk composition as T_L^0, and the solidus temperature T_S. Assuming fractional crystallization, the liquidus temperature varies with time as the liquid composition is modified as the solid crystals are stored in the sediment pile, thereby isolated from the remaining liquid. Let us define the solid fraction $\chi(h) = h/H_0$. We assume that the liquidus temperature decreases linearly with χ from the initial liquidus temperature to the solidus temperature, and that the released latent heat of crystallization is

proportional to the rate of change of the solid fraction, $\dot{\chi}$,

$$T_L(\chi) = T_L^0 - \chi(T_L^0 - T_S)\,. \tag{4.6}$$

$$L = \dot{\chi}\mathcal{L}\,, \tag{4.7}$$

where $\mathcal{L}$ denotes the latent heat of crystallization per unit mass of fluid. Note that χ denotes the solid fraction in the original volume of the chamber, i.e. it accounts for the sediment pile, not to be confused with current crystalinity in the dominantly liquid region. Eq. (4.6) provides the last desired quantity, $T_L(t)$, when $\chi(h(t))$ is evaluated as a function of time. The evolution of the sediment pile height, $h(t)$, couples the thermal model with the previously described model of crystal growth kinetics.

4.1.1 Energy balance

We can obtain a rough first order estimate for the evolution of temperature variables $T_B(t)$ and $\Delta T(t)$ by addressing the energy balance inside the chamber, which can be compactly written as

$$(H_0 - h)\rho_F c_p \frac{\mathrm{d}T_B}{\mathrm{d}t} = -\mathcal{F} + \rho_F \mathcal{L}\dot{h}\,, \tag{4.8}$$

where we employed the quasi-steady state implication equating the production rate of crystals with the sedimentation rate. By imposing an ad hoc constant heat flux $\mathcal{F}$ (heat flux estimate from volcanic calderas can be found in, e.g., Carrigan [1988]), we can consistently solve Eq. (4.8) with supplied increasing sediment height h and rate of sedimentation $\dot{h}$, and thus decreasing temperature contrast ΔT following Eq. (4.5)), and decreasing liquidus temperature according to Eq. (4.6). Varying fluid conditions will be reflected in the evolution of the mean crystal radius with the height of the sediment.

Conclusion

In this thesis, we revisited the problem of thermal convection inside magma chambers through the optics of microstructural records of igneous intrusions. We have built upon theoretical groundwork laid by Jarvis and Woods and have endowed the parametrized model of a magma chamber with TBL dynamics, a more complex parametrization of settling dynamics, and more realistic nucleation and growth kinetics. We developed a quasi-steady state solver that computes the crystal size distributions in TBL, bulk, and sediment for a given setup of the chamber.

We analyzed the TBL process and found out that the inflow distribution signature is observable in the sediment merely for small temperature contrasts (i.e, $\Delta T < 1$ K) and has a marginal impact on the mean crystal radius. Furthermore, we performed a thorough parametric study, which led to the identification of four distinct end-members (pure dust-like, dust-like dominance, stone-like dominance, and pure stone-like regimes) for the distribution in the sediment, each directly reflecting the prevailing settling mechanism. This is a key result as it indicates that it is necessary to look not only at the characteristic crystal size (i.e., the mean radius) but rather at the shape of the observed distributions. The dependence of the mean radius on the convective vigor, controled by the unknown temperature contrast ΔT, is rather weak - this is a disappointing result, but the absence of the predicted quasi-Dirac distribution, associated with purely stone-like regime (essentially Stokes sinking), suggests that thermal convection inside magma chambers is vigorous.

Furthermore, we outlined our future ambitions - the presented model is ready to be coupled with the thermal evolution of the overlying region through a 1D heat equation. This will allow us in the future to capture the evolution of the mean crystal radius with the depth of the sediment, something that can be directly compared to observations.

Attachment

The code `1DNGMC` is written in *Python 3* and is divided into several modules:

- module `mPar.py`: contains classes with parameters, constants, and boolean switches for individual computational methods (0-generation vs. step-by-step, method of distributions vs. crystal tracing, linear vs. Hortian kinetic laws, settling dynamics)
- module `mFunc.py`: contains auxiliary functions, developed data structures, classes, and saving procedures
- module `mPhase.py`: contains solvers for the TBL and bulk processes, computes steady state crystal size distributions $\Phi_{\text{tbl}}(a)$, $\Phi_{\text{sed}}(a)$, and $\Phi_{\text{blk}}(a)$
- module `mPlot.py`: responsible for the post-processing of an individual run
- module `main.py`: unit containing the main solidification loop, responsible for all apriori and aposteriori calculations

The developed code either computes the snapshot (or evolution, for constant ΔT and T_B so far) for a given setup. Additionally, the code is automatized for parallel computations of an arbitrary number of models, including automatized post-processing (modules `mCombs.py` and `mRuns.py`), in the bash script `exe.sh`.

Bibliography

Guenter Ahlers, Siegfried Grossmann, and Detlef Lohse. Heat transfer and large scale dynamics in turbulent rayleigh-bénard convection. *Reviews of Modern Physics*, 81(2):503–537, April 2009. ISSN 1539-0756. doi: 10.1103/revmodphys.81.503.

Geneviève Brandeis and Bruce Marsh. The convective liquidus in a solidifying magma chamber - a fluid dynamic investigation. *Nature*, 339, 07 1989. doi: 10.1038/339613a0.

Charles R Carrigan. Biot number and thermos bottle effect: Implications for magma-chamber convection. *Geology*, 16(9):771, 1988.

Eric Dowty. Chapter 10. crystal growth and nucleation theory and the numerical simulation of igneous crystallization. In *Physics of Magmatic Processes*, pages 419–486. Princeton University Press, Princeton, December 1980.

Frank Press. *Understanding Earth*. W.H. Freeman, New York, NY, 3 edition, September 2000.

Marian B Holness. Microstructural evidence for the fluid dynamical behaviour in vertically and laterally propagated dykes of the british and irish paleogene igneous province. *J. Petrol.*, 63(11), November 2022.

Marian B. Holness, Robert Farr, and Jerome A. Neufeld. Crystal settling and convection in the shiant isles main sill. *Contributions to Mineralogy and Petrology*, 172(1), January 2017. ISSN 1432-0967. doi: 10.1007/s00410-016-1325-x.

M. Hort. Cooling and crystallization in sheet-like magma bodies revisited. *Journal of Volcanology and Geothermal Research*, 76(3):297–317, 1997. ISSN 0377-0273. doi: https://doi.org/10.1016/S0377-0273(96)00079-0.

Herbert E. Huppert and J. Stewart Turner. Comments on 'On Convective Style and Vigor in Sheet-like Magma Chambers' by Bruce D. Marsh. *Journal of Petrology*, 32(4):851–854, 08 1991. ISSN 0022-3530. doi: 10.1093/petrology/32.4.851.

Richard A. Jarvis and Andrew W. Woods. The nucleation, growth and settling of crystals from a turbulently convecting fluid. *Journal of Fluid Mechanics*, 273:83–107, 1994. doi: 10.1017/S0022112094001850.

Robert H Kraichnan. Turbulent thermal convection at arbitrary prandtl number. *Phys. Fluids*, 5(11):1374–1389, November 1962.

B.D. Marsh. Crystal capture, sorting, and retention in convecting magma. 1990. ISSN 0072-1077. doi: 10.1130/spe253-p399.

Bruce Marsh. Magma chambers. *Annual Review of Earth and Planetary Sciences*, 17:439–472, 05 1989a. doi: 10.1146/annurev.earth.17.1.439.

Bruce D. Marsh. Reply. *Journal of Petrology*, 32(4):855–860, 08 1991. ISSN 0022-3530. doi: 10.1093/petrology/32.4.855.

Brude D. Marsh. On Convective Style and Vigor in Sheet-like Magma Chambers. *Journal of Petrology*, 30(3):479–530, 06 1989b. ISSN 0022-3530. doi: 10.1093/petrology/30.3.479.

Daniel Martin and Roger Nokes. Crystal settling in a vigorously convecting magma chamber. *Nature*, 332(6164):534–536, April 1988. ISSN 1476-4687. doi: 10.1038/332534a0.

Daniel Martin and Roger Nokes. A Fluid-Dynamical Study of Crystal Settling in Convecting Magmas. *Journal of Petrology*, 30(6):1471–1500, 12 1989. ISSN 0022-3530. doi: 10.1093/petrology/30.6.1471.

Huaiwei Ni, Hejiu Hui, and Gerd Steinle-Neumann. Transport properties of silicate melts. *Reviews of Geophysics*, 53(3):715–744, August 2015. ISSN 1944-9208. doi: 10.1002/2015rg000485.

Vojtěch Patočka, Nicola Tosi, and Enrico Calzavarini. Residence time of inertial particles in 3d thermal convection: Implications for magma reservoirs. *Earth and Planetary Science Letters*, 591:117622, 2022. ISSN 0012-821X. doi: https://doi.org/10.1016/j.epsl.2022.117622.

G.W. Scherer and D.R. Uhlmann. Effects of phase separation on crystallization behavior. *Journal of Non-Crystalline Solids*, 21(2):199–213, July 1976. ISSN 0022-3093. doi: 10.1016/0022-3093(76)90041-7.

John M. Sinton and Robert S. Detrick. Mid-ocean ridge magma chambers. *Journal of Geophysical Research: Solid Earth*, 97(B1):197–216, 1992. doi: https://doi.org/10.1029/91JB02508.

Viatcheslav S. Solomatov. Magma oceans. *Treatise on Geophysics*, 9:91–119, 2004.

Tilman Spohn, Matthias Hort, and Heide Fischer. Numerical simulation of the crystallization of multicomponent melts in thin dikes or sills: 1. the liquidus phase. *Journal of Geophysical Research: Solid Earth*, 93(B5):4880–4894, May 1988. ISSN 0148-0227. doi: 10.1029/jb093ib05p04880.

Donald Turcotte and Gerald Schubert. *Geodynamics*. Cambridge University Press, 3 edition, 2014.

List of Figures

List of Tables